Towards the photocatalytic production of cinnamaldehyde with phosphorous-tailored graphitic-like carbon nitride

María Alejandra Quintana, Alba Picón, María Ángeles Martín-Lara, Mónica Calero, Mario J. Muñoz-Batista [*], Rafael R. Solís [*]

Department of Chemical Engineering, University of Granada, Avda. Fuentenueva s/n, Granada 18071, Spain

ARTICLE INFO

ABSTRACT

Photocatalysis has emerged as an environmentally friendly technology to develop selective reactions such as the oxidation of alcohol to aldehydes. Graphitic carbon nitride (CN) is a metal-free polymeric structure easily photoactivated under radiation. This work focuses on the enhancement of the photocatalytic activity of bare CN by doping it with phosphorous (P-CN). Different doping levels of P (2–12 wt.) have been explored and the samples were fully characterized by XRD, FTIR, N_2 physisorption, elemental analysis, XPS, DRS-UV–visible, and photoluminescence. A better activity and enhanced selectivity were observed in the P-CN samples if compared to the undoped CN in the oxidation of cinnamyl alcohol to cinnamaldehyde in aqueous solution. The presence of P was demonstrated to contribute to a better delocalization of photo-generated charges. Moreover, the reactivity and selectivity of the CN and P-CN samples were analyzed in water-acetonitrile mixtures, appreciating a better selectivity in the presence of acetonitrile to the detriment of the conversion of the cinnamyl alcohol. The photocatalytic oxidation mechanism over P-CN in aqueous media has been tentatively proposed based on the influence of the reactive oxidative species generated in the process by chemical scavenger tests. They suggested the contribution of superoxide radicals with more selectivity than the photo-generated holes, the second reactive species of importance in the overall oxidation scheme. The contribution of hydroxyl radicals was discharged since its presence was negligible in a probe test based on the formation of 2-hydroxy-terephthalic acid.

1. Introduction

The oxidation of alcohols to aldehydes is one of the most important reactions in organic chemistry oriented to the high-scale production of added-value organics, as happens in the pharmaceutical industry. Cinnamaldehyde is one example of these substances, widely used in cosmetics [1], as a food additive [2,3] taking advantage of its antibacterial and antifungal activity [4], or as an ingredient of natural formulas for insecticides [5]. The synthesis of cinnamaldehyde at an industrial scale has been successfully carried out under catalytic oxidation with O_2 with noble metals such as Pd [6] or Pt [7]. Diverse techniques are subsequently implemented to purify the components of the mixture of the reaction, also carried out when obtaining form essential oil of cinnamon [8]. Among the available techniques, the most popular include hydrodistillation [9], steam distillation [10], microwave-assisted hydrodistillation [11], sonodistillation [12], or column chromatographic techniques [13].

Recently, the oxidation of alcohols to aldehydes through photocatalysis has emerged as an environmentally friendly alternative to traditional routes due to the mild pressure and temperature conditions [14–16]. Moreover, photocatalysis can be triggered with solar radiation which justifies the sustainability of the radiation consumption. The selectivity of the photocatalytic oxidation of alcohols to aldehydes has been reported to reach the highest values in the presence of an inert organic solvent, acetonitrile being the most popular [16]. Nonetheless, the disposal of organic solvents is an issue of major concern from an environmental point of view. The development of these reactions in water may solve this problem; however, the presence of water can trigger the production of unselective hydroxyl radicals, contributing to poor selectivity control [17,18]. This drawback can be addressed with a proper catalyst design. In this sense, graphitic carbon nitride (g-C_3N_4) has shown a competitive bandgap alignment for this purpose since the energy of the conduction band enables the formation of photogenerated electrons with enough energy to release the reduction of adsorbent O_2

---

molecules to superoxide radical. However, due to the energetic value of the valence band, the potential of the photogenerated holes in the valence band is not enough to oxidize H_2O molecules to release the formation of hydroxyl radicals [14]. The use of g-C_3N_4 has been demonstrated as a sustainable photocatalyst for the photoproduction of added-value chemicals [19]. The doping of the polymeric structure of g-C_3N_4 with non-metal elements has been used as an efficient strategy to boost the activity and/or modulate the selectivity of certain reactions [20,21]. Among the different elements used as dopant agents, the effects of phosphorous doping in g-C_3N_4 applied to the photoproduction of organic substances are the least researched to date. The doping of g-C_3N_4 with $NH_4(H_2PO_4)$ has been reported as efficient in raising the selectivity to the detriment of the precursor conversion during the photoproduction of aldehydes from the oxidation of benzyl alcohol, 4-methoxy benzyl alcohol, or piperonyl alcohol [22]. In other work, g-C_3N_4 was doped with H_3PO_4, and Pd nanoparticles were also deposited on the surface. Both modifications enabled to reach a high yield of aldehydes production from their benzyl alcohol derivatives, using acetonitrile as solvent and H_2O_2 as an oxidant agent [23].

This work reports the study of P doping onto g-C_3N_4, using sodium phosphate as a doping agent, for the photocatalytic production of cinnamaldehyde in an aqueous solution. Different P doping dosages have been investigated within 2–12% (wt.). The crystalline, morphological, textural, and optical properties were characterized by diverse techniques such as XRD, FTIR, N_2 physisorption, XPS, elemental analysis, DRS-UV–visible, and photoluminescence. The behavior in terms of conversion and selectivity during the oxidation of cinnamyl alcohol to cinnamaldehyde has been investigated in an aqueous solution. The undoped and the P-doped samples with the best selectivity were selected to investigate the effect of acetonitrile as the solvent, in acetonitrile-water mixtures. Finally, the tentative mechanism of oxidation species involved in the process was assessed by using chemical scavengers to assess the effects of superoxide radical (N_2, p-benzoquinone, tiron), hydroxyl radical (tertbutyl alcohol), and photogenerated holes (oxalic acid, EDTA).

2. Experimental section

2.1. Materials and synthesis of the P-CN samples

All the chemicals used were analytical grade, purchased from Merck®, and used as received. For liquid chromatographic analyses, HPLC-grade acetonitrile was used as a mobile phase. Ultrapure water (18.2 MΩ cm) from a Direct-Q®-UV device (Millipore®) was used for the preparation of all the solutions.

The bare graphitic carbon nitride (CN) was prepared by thermal polymerization of melamine (>99%), under an N_2 atmosphere (100 mL min^{-1}) at 550 °C (heating rate, 10 °C min^{-1}) for 1 h. The P-doping of graphitic carbon nitride samples (P-CN) was carried out in a second post-treatment step [24], as illustrated in Fig. 1. A certain amount of P (2–12% wt. concerning the CN quantity) was added as sodium phosphate (65–70% P_2O_5 basis) to 20 mL of ultrapure water and kept under stirring for 2 h. The suspension was thereafter subjected to evaporation by heating at 100 °C until the complete removal of water. The powder was next treated thermally under N_2 atmosphere (100 mL min^{-1}) at 550 °C (heating rate, 10 °C min^{-1}) during 2 h. The resulting brownish powder was ground in a mortar. The samples were labeled as P-CN-X% where X means the doping P percentage (wt.).

2.2. Characterization of the P-CN samples

The crystallinity was analyzed by X-ray diffraction in a Bruker D8 Discover device working with a Pilatus 3 R 100 K-A detector using Cu Kα radiation (1.5406 Å). The diffractograms were registered within a 2θ range of 5–65° at a rate of 0.034° min^{-1}. The freeware QualX® [25] and the Crystal Open Database (COD) were used for the processing of the diffractograms. The crystallite size was estimated by Scherrer's equation from the most intense peak and the interlayer spacing was calculated from the maximum of the (002) peak. The relation $L_{crystal}/d_{layer}$ was used as a rough approximation of the number of layers estimation [26].

The structural properties were studied by Fourier Transform InfraRed (FTIR) spectroscopy equipped with Attenuated Total Reflectance. The FTIR spectra were recorded in Perkin-Elmer equipment, model Spectrum65, within 400–4000 cm^{-1}.

The elemental composition was analyzed in a TrueSpec® Micro CHNS analyzer from Leco instruments. The chemistry of the surface was analyzed by X-ray Photoelectron Spectroscopy (XPS) in a Kratos AXIS UltraDLD device equipped with an X-ray source from Al Kα. The registered spectra were corrected to C_{1s} peak of adventitious carbon as referenced, ascribed to 284.6 eV. The treatment of the data and the deconvolution of the spectra were carried out with the software XPSpeak 4.1®, applying a Shirley background correction for the baseline definition. The chemical environment of C and P was further studied by solid state Magic Angle Spinning (MAS) Nuclear Magnetic Resonance (NMR) in a Bruker Advance NMR spectrometer of 500 MHz equipped with a 4 mm Cross-Polarization (CP) MAS detector. In the case of ^{13}C spectra, CP-MAS experiments were conducted at 10 kHz. For ^{31}P the MAS, tests were carried out at 12 kHz.

The morphology and element distribution in the nanoparticles were studied by High Resolution Scanning Transmission Electron Microscopy (HR-STEM) imaging in a Thermo Scientific™ Talos™ F200X (200 kV) equipped with High-angle annular dark-field imaging (HAADF) detector and Energy Dispersive X-Ray spectroscopy (EDX) microanalysis.

The optical absorption and reflection of the samples were studied by Diffuse Reflectance Spectroscopy (DRS) in the UV–visible region using a Varian Cary 5E spectrophotometer. The bandgap value was estimated from the Kubelka-Munk Function, e.g. $F(R_\infty)$, applying the Tauc plot method assuming indirect electron transitions in the semiconductors
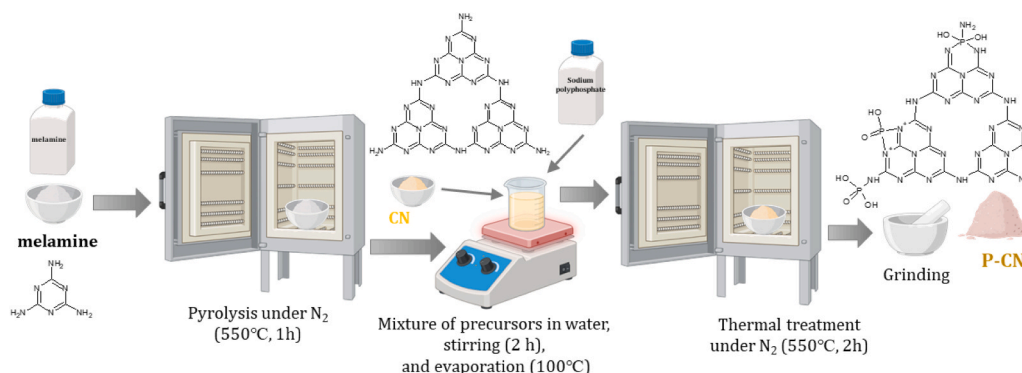

Fig. 1. Schematic representation of the synthesis steps of CN and P-CN samples.

[27,28]. The photoluminescence (PL) technique was used for the analysis of the recombination rate of the samples. The PL spectra were obtained in a Varian Cary fluorescence spectrometer under an excitation wavelength of 365 nm (slit 2.5 nm) and monitored the emission signal within 400–600 nm (slit 2.5 nm).

2.3. Photocatalytic tests of cinnamaldehyde production

The photocatalytic activity of the prepared samples was evaluated in the selective oxidation of cinnamyl alcohol (CA) to cinnamaldehyde (CD). The tests were carried out in a photoreactor equipped with two UVA lamps emitting at 365 nm (9 W each). The lamps were placed in the inner space of an annular photoreactor in whose inner space was circulating the aqueous solution with the suspended catalyst. An auxiliary jacketed tank contained the solution of cinnamyl alcohol with the catalyst and was pumped and recirculated to the photoreactor. The temperature was controlled to 20 °C by cooling with water in the jacketed space of the auxiliary tank. A detailed scheme of the setup is available in previous work [29]. Alternatively, lamps simulating daylight radiation were used to test the activity of the photocatalyst in the visible region (Philips). The spectrum was characterized with the help of a BLACK-Comet UV–visible spectroradiometer (StellarNet Inc., Florida, USA). Air was bubbled in the auxiliary tank to ensure O_2 saturation. The photocatalytic reaction started with the loading of 350 mL of CA 1 mM to the auxiliary tank and the catalyst at a dose of 0.5 g L^{-1} until a homogeneous slurry was obtained which was pumped into the annular space of the photoreactor. Before the irradiation, a 30-minute adsorption step was carried out in the darkness. Then, the laps were switched on and samples were carried out regularly. The photocatalyst was removed by syringe filters (Millex PVDF, 0.45 μm).

The concentration of cinnamyl alcohol and cinnamaldehyde was determined by High-Pressure Liquid Chromatography (HPLC) coupled with photodiode array (PDA) detection. An Alliance e2695 HPLC system from Waters™, coupled to a 2998 PDA detector. The stationary phase used for the separation of CA and CD was a Zorbax Bonus-RP column (5 μm, 4.6 ×150 mm). The mobile phase, pumped at 1 mL min^{-1} under the isocratic mode, consisted of a mixture of 40% (v/v) acetonitrile and 60% (v/v) ultrapure water acidified with 0.1% (v/v) of trifluoroacetic acid. The injection volume was 50 μL. The quantification was carried out at 240 nm for CA and 331 for CD.

The temporal evolution of CA depletion was fitted to a pseudo-first order kinetics, and the observed constant (k_{CA}) was used as a mere comparison tool among the prepared catalysts. The selectivity towards cinnamaldehyde was calculated from the CD and CA profiles, and an average value (S_{CD}) during the whole period tested was calculated. The quantum efficiency (Q_E) of CA photo-degradation was estimated, following the IUPAC's recommendations [30–32] which defines the Q_E as the ratio of the number of molecules reacting through the reaction rate ($r_{CA,0}$), by the photon absorption rate (LVRPA, $e^{\alpha,\nu}$), i.e. the number of the photons interacting with the catalyst [33]:

$$Q_E = \frac{r_{CA_0}(\text{mol}\,m^{-3}\ s^{-1})}{e^{\alpha,\nu}(\text{Einstein}\,m^{-3}\ s^{-1})} \tag{1}$$

where $r_{CA,0}$ was estimated from the pseudo-first order kinetics ($r_{CA,0} = k_{CA} \cdot C_{CA,0}$). The determination of the photon absorption rate ($e^{\alpha,\nu}$), and the radiative transfer equation (RTE) was solved considering the geometry of the used photoreactor [29]. The optical properties were determined by the DRS-UV–visible of the catalytic suspensions. Detailed descriptions of the mathematical procedure for both optical properties and photon rate estimations are provided in previous works [29,34]. Fig. 2 provides the LVRPA profiles for the different P-CN samples and the undoped CN reference.

The behavior under visible radiation was conducted using a daylight simulated radiation with a commercial lamp (Sylvania® F6W/T5/ 54–765, emitting radiation >400 nm, 6 W) in a modified reaction system in which the lamp was inserted in a tubular photoreactor, see details in a previous work [34].

The contribution of the oxidative species involved in the oxidation of cinnamyl alcohol during the photocatalytic process was studied by the addition of chemical scavengers [35–37]. The role played by superoxide radical was evaluated by adding p-benzoquinone (p-BZQ, 1 mM), disodium 4,5-dihydroxy-1,3-benzenedisulfonate (tiron, 1 mM) or bubbling N_2, the contribution of hydroxyl radicals by adding tert-butyl alcohol (TBA, 10 mM), the role played by the photo-generated holes was suppressed under the presence of oxalic acid (10 mM) or ethylenediaminetetraacetic acid (EDTA, 1 mM), and the influence of single oxygen was assessed by adding L-histidine (1 mM). These assays were conducted following the same procedure described before, but by
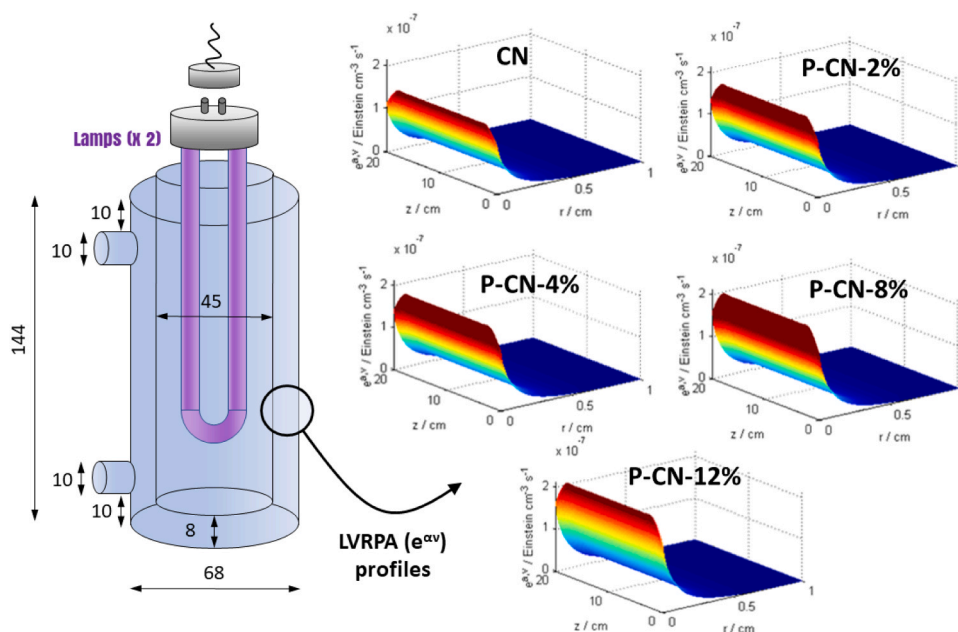

Fig. 2. Local Volume Rate of Photon Absorption (LVRPA, $e^{\alpha,\nu}$) in the annular space of the photoreactor (left image, dimensions in mm) for the different P-CN samples.

adding the scavenger to the solution the pH was adjusted to the value of the blank test under the addition NaOH and/or HCl solutions 1 M. The role played by the HO$^\bullet$ was additionally assessed by an indirect probe method based on terephthalic acid (TPA) [38,39]. Non-fluorescent terephthalic acid traps HO$^\bullet$ releasing the formation of the fluorescent 2-hydroxy-terephthalic acid (2-HO-TPA), which can be monitored over time as an indirect indicator of the HO$^\bullet$ present in the solution. Two tests with 2-HO-TPA (1 mM) in the presence and absence of cinnamyl alcohol were carried out and compared [40]. The analysis of 2-HO-TPA was conducted in a Varian Cary fluorescence spectrometer with an excitation wavelength of 315 nm (slit 2.5 nm) and the emission spectra recorded within 360–600 nm (slit 2.5 nm), whose maximum peak was located at 420 nm. The peak area was correlated with the concentration of the standard 2-HO-TPA solution within 0.5 and 5 μM. The limit of detection of 2-HO-TPA was estimated at 0.21 mM.

The transformation products during the photocatalytic oxidation of cinnamyl alcohol with P-CN were identified by liquid chromatography coupled to electrospray ionization under positive mode and mass spectrometry detection with a quadrupole time-of-flight, LC-ESI(+)-QTOF. The chromatographic separation was carried out in an ultra-high-pressure Acquity UPLC, H Class of Waters™, equipped with PDA detection. The ionization was carried out in a Zspray™ from Waters and the high-resolution mass spectrometry in a QTOF Triwave® Waters™, Synapt G2 model. The acquisition conditions were as follows: 3500 V capillary voltage, collision energy, X eV, *m/z* range from 50 to 1000. The identification of the transformation products was carried out based on MS spectra of precursor using the software MassLynx.

3. Results and discussion

3.1. Characterization of the P-CN samples

Fig. 3 depicts the structural modifications suffered by the graphitic carbon nitride sample before and after doping with sodium polyphosphate. Fig. 3A depicts the XRD patterns of bare CN and P-doped samples at two P loadings. The graphitic carbon nitride structure reports two crystalline peaks. The condensation of the precursor, i.e. melamine, conducts the formation of tris-s-triazine units distributed in plates of a certain number of layers [41,42]. As a consequence, a main and intensive peak located at 27° is described, corresponding to the (002) plane which appears due to the interplanar aromatic layers from π-π * interactions of the heptazine rings [43]. The polymerization temperature is linked to the sharpness of this peak and, the number of layers, within 22–31 at condensation temperatures of 500 and 600 °C, respectively, is expected under air atmosphere [44]. A secondary peak, barely defined, placed at ca. 13° is defined by the (100) plane, a consequence of the intralayer spacing of the heptazine rings [45].

The modification of the g-C$_3$N$_4$ structure leads to considerable modification of the (002) peak, as a consequence of the alteration of the number of layers attached to the structure. For that reason, the decrease of the (002) peak is frequently analyzed as the degree of modification of the layered structure [46]. Thus, doping with a low P dose, i.e. P-CN-4%, depicts a decrease of the (002) peak, suggesting a considerable modification of the layered interactions, probably due to the incorporation of phosphate groups. Some previous works have reported a migration of the (002) peak to lower values, suggesting the incorporation of phosphate groups into the interlayers of the graphitic carbon structure, following a sandwich structure [47]. However, probably due to the post-treatment doping scheme followed in this work, it was not the case. The location of (002) of CN and P-CN-4% was roughly the same, around 27.4°, which provides evidence of a lack of modification of the layer spacing, discharging the incorporation of P between layers since the interlayer space slightly decreased (see Table 1). Accordingly, P is expected to be incorporated in the external faces of the plates or the heptazine rings. A further rise of P amount destroyed the layered nature of CN, as depicted for P-CN-12%, defining a crystalline structure of phosphate-based nitrogen organic compounds that were not possible to identify due to the complexity of plausible generated species.

The doping with phosphate also led to considerable changes in the FTIR spectra as displayed in Fig. 3B. The absorption characteristics of P-CN samples are similar to those of CN, suggesting that the structure of g-C$_3$N$_4$ has not been changed after P doping, at least at P doses below 4%. At high P doping, some changes in the fingerprint of FTIR spectra are envisaged. A wide band located within 3000–3300 cm^{-1} due to the vibration of terminal N–H and O–H stretching, which can be associated with the primary amine (-NH$_2$) and water molecules adsorbed on the surface of the material [48], is defined in the undoped CN sample. The increase in P dose led to a considerable decrease in this band, suggesting that P incorporation affected the terminal -NH$_x$ groups. The aromatic tri-s-triazine rings lead to different peaks. Thus, the secondary nitrogen (N$_{2 C}$) and tertiary nitrogen (N$_{3 C}$) were conducted to well-defined peaks located at 1225 and 1312 cm^{-1}, respectively [49]. Moreover, the peaks located at 1391, 1450, 1537, and 1622 cm^{-1} can be attributed to the aromatic C-N vibration [42,50,51]. A strong peak at 811 cm^{-1} appears
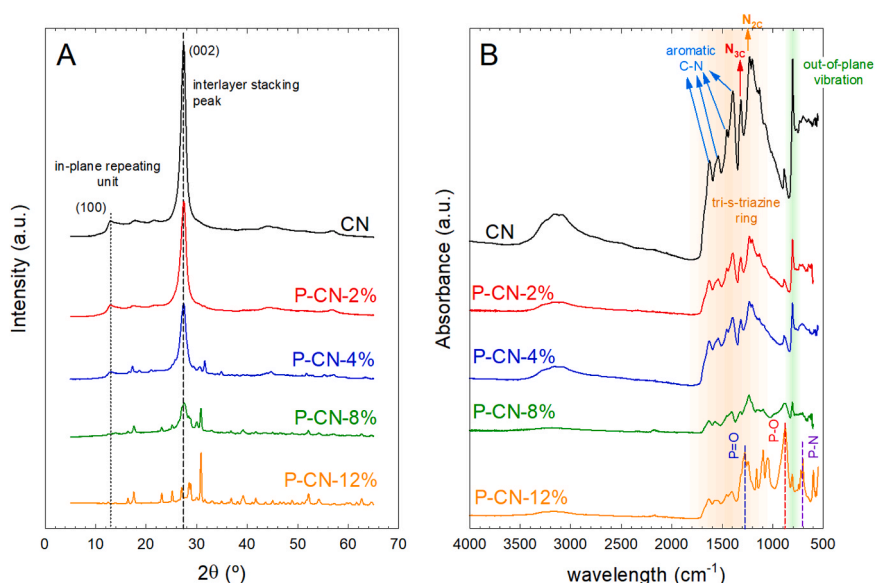

Fig. 3. XRD diffractograms (A) and FTIR spectra (B) of the P-CN samples.

Table 1
Crystal and textural properties, elemental composition, and optical properties of P-CN samples.

Sample	$L_{crystal}$ (nm)	d_{layer} (Å)	n	S_{BET} (m^2 g^{-1})	V_T (cm^3 g^{-1})	N_{EA} (wt%)	C_{EA} (wt%)	N/C_{EA} (at.)	O_{XPS} (wt%)	P_{XPS} (wt%)	E_{BG} (eV)
CN	5.77	3.250	18	9.1	0.050	60.8	35.1	1.485	4.8	-	2.7
P-CN-2%	7.37	3.245	22	8.4	0.035	53.0	30.6	1.499	8.8	1.78	2.6
P-CN-4%	7.62	3.250	29	4.2	0.018	50.4	28.7	1.505	8.2	4.04	2.6
P-CN-8%	6.62	3.236	-	8.7	0.047	36.9	19.6	1.600	16.3	7.84	2.5
P-CN-12%	19.45	3.131	-	6.6	0.027	12.3	6.7	1.574	24.3	10.6	2.0

$L_{crystal}$, crystallite size from the (002) peak by Scherrer's equation; d_{layer}, interlayer spacing from the (002) peak; n, number of layers; S_{BET}, specific total surface area obtained from the BET method; V_T, total pore volume obtained from the N_2 uptake at $p/p_0 \sim 0.99$; C and N composition from elemental analysis (EA); N/C_{EA}, the atomic N/C ratio by elemental analysis; O and P content from XPS analysis; and E_{BG}, bandgap energy estimated from the Tauc plot method.

due to the out-plane vibration of the heptazine rings [49]. The presence of P led to the decrease and definition of the above-mentioned peaks of the bare CN sample. Significantly, the P doping contributed to an exfoliation effect of graphitic layers, corroborated by a considerable decrease in the out-of-plane vibration peak at 811 cm^{-1} [52]. When doping with over 8% of P, some new peaks appeared as a consequence of the significant amount of P in the structure. At 1271 cm^{-1} appears a peak that can be attributed to the stretching vibration mode of the P = O bond [53]. A plausible bonding as P = N was not reflected in the FTIR spectra, as no peaks centered at around 1336 and 1430 cm^{-1} were observed [53]. Additionally, the peak detected at 1094 cm^{-1} could be interpreted as the P$^+$-O- vibration in phosphate esters, in polyphosphate chain P-O-P [54,55]. The N-P vibration usually conducts to an FTIR peak centered at 700 cm^{-1} [54,56,57] which is consistent with the peak located at 701 cm^{-1} registered in this work at high P dosages. In brief, the above analysis suggests that P was successfully introduced in the g-C$_3$N$_4$ structure without changing the original framework at low doping doses, contributing just to an exfoliation effect and a plausible bonding of P groups to the N atoms.

The surface chemistry of the doped CN with sodium polyphosphate was analyzed by XPS. The sample with the optimum photocatalytic behavior, i.e. P-CN-4%, was selected for the evaluation of the chemical interaction type with carbon nitride. The XPS spectra are illustrated in Fig. 4. The C$_1$ s peak of g-C$_3$N$_4$ is traditionally deconvoluted in three main contributions, i.e. a peak of sp^2 bonds representative of N = C-N bonds (287.7 eV), a peak of sp^3 carbon in C-C/C-N bonds (285.6 eV),

and a peak of sp^2 carbon bonds of C-C/C=C (284.4 eV) [34,58]. From the C$_1$ s spectrum, the sp^2 N = C-N contribution counts as 59% of the whole area. In our previous works of the undoped sample [34,59], that means the CN sample, the sp^2 carbon of N = C-N considerably outlines the other two contributions, being 71% of the area contribution. The P doping forced a considerable decrease in this contribution, suggesting a plausible attack of P to the C positions and replacement as reported in the literature [60–62]. The diminishing contribution of the aromatic N = C-N could be considered the first evidence of P attacking to C positions. The N$_1$ s region of graphitic carbon nitride can be interpreted as the contribution of three bonds, namely tertiary N from (C)$_3$–N rings (N$_{3 C}$, 399.9 eV), sp^2-bonded in the form of N–C≡N (N$_{2 C}$, 398.4 eV), and terminal -NH$_x$ groups (400.8 eV) [44,63–66]. The N$_{2 C}$ and terminal -NH$_x$ contributions in the P-CN-4% sample are lower in importance to the N$_{3 C}$ peak if compared to the bare CN blank reported in our previous works [34,59]. This evidence could be interpreted as a second fact of P replacing with C atoms, leading to a higher proportion of N$_{3 C}$. The high-resolution peak P$_{2p}$ spectrum has been deconvoluted in three plausible contributions: P–C, P–N, and P-O bonding at 132.6 eV, 133.7 eV, and 135.0 eV, respectively, according to the literature [67]. As portrayed in Fig. 4, the deconvolution led to a majority contribution of P-N although the contribution of P-O was lower but considerable. However, the contribution of P-C was negligible. The presence of the P-N bond suggests the anchorage of phosphate to nitrogen, either due to the reaction with terminal amino groups [68–70], supported by the decrease of the -NH$_x$ stretching band in FTIR, or by the replacement of C in triazine rings atoms [62,71,72]. It has been reported a large nitrophilicity by P atoms, which provide stable P-N polymers. However, the larger bond length of P-N (150–170 pm) if compared to C-N in carbon nitride (135 pm) compromises the planar structure of P-CN [68]. Moreover, due to the possibility of coordination of P with O, the presence of P-O cannot be discharged. The presence of P-O binging may be linked to some terminal hydroxyl groups. The superficial quantification of P in P-CN-4% revealed a 4.04% (wt.) of P. The XPS analysis also revealed the presence of Na in the structure. From the results of the Na$_1$ s spectrum (results not shown), a plausible coordination of Na$^+$ with N atoms into the interstitial heptazine rings can be deduced. It has been reported that the calcination process in the presence of sodium tripolyphosphate promotes this coordination due to the strong ability of N atoms with lone-pair electrons towards metal ions [24], triggered by the lower electronegativity of N if compared to O. Finally, the doping with P increased the oxygen content, from 4.8% (wt.) of the bare CN to 8.2% (wt.) of P-CN-4%. In the O$_1$ s region, the main peak observed originated from the sum of two plausible contributions located at 533 and 531 eV, assigned to, respectively, terminal -HO [73] and O^{2-} of phosphate environment [74] or C=O [73]. Surface O content, see Table 1, was raised with the increase of P doping, which suggests the binding of P to O, as discussed previously.

Solid-state ^{13}C and ^{31}P MAS NMR were carried out to verify the changes in the chemical environment of C and P of g-C$_3$N$_4$ after doping. As illustrated in Fig. 5, the ^{13}C NMR spectrum was modified after the incorporation of P in the graphitic framework. Both spectra depicted two well-defined signals at ~154 and ~162 ppm, which can be attributed respectively to the bay site of C$_3$N corresponding to internal C atoms in
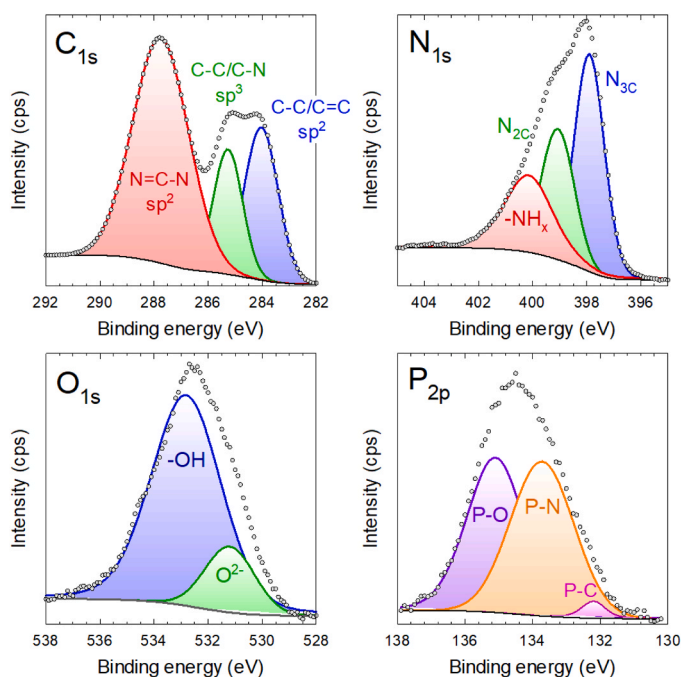

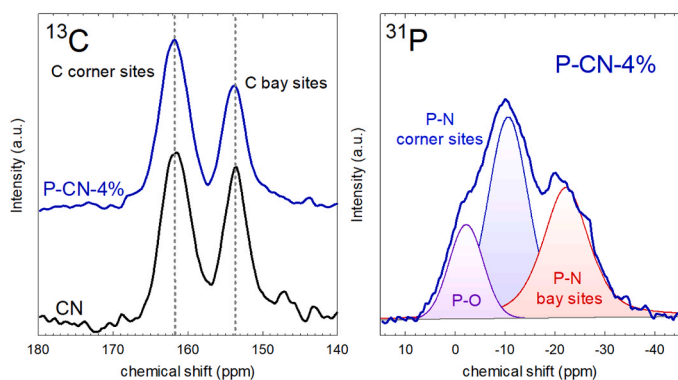**Fig. 4.** XPS spectra of high-resolution elements (C, N, O, and P) of P-CN-4% sample.

Fig. 5. ^{13}C CP-MAS NMR spectra of CN and P-CN-4% and ^{31}P MAS NMR spectrum of P-CN-4%.

tri-s-triazine rings, and the corner site C_2N-NH_x atoms attributable to those C atoms connected next to bridging $-NH_x$ [75–77]. There was no appreciated signal a 149 ppm, assignable to cyanuric groups, $-C\equiv N$ [75]. According to the ^{13}C spectra of unmodified CN, the two contributions display a very similar intensity, being the corner contribution slightly higher. The P-CN-4% displayed a quite similar ^{13}C spectrum, revealing, therefore, a well-preserved framework. However, the doping with P promoted the decrease of the contribution of the bay sites, which means the peak located at ~154 ppm diminished its intensity, providing

evidence of partial substitution of P atoms in the corner bay C of the g-C_3N_4 skeleton. The ^{31}P MAS NMR spectrum of P-CN-4%, see Fig. 5, described a broad peak due to the low P amount and the presence of multiple P-containing species [76]. The signals at roughly − 10 and − 20 ppm may be associated with the chemical environment of corner and bay phosphorus sites, respectively, whereas a signal at around 0 ppm can be ascribed to P-O at some edge terminal positions [78,79]. Taking this information into account, the ^{31}P spectra of P-CN-4% were deconvoluted in three contributions, obtaining deconvoluted peaks centered at − 2.2 ppm for P-O, − 10.6 ppm for corner, and − 22.2 ppm for bay positions. Therefore, similar conclusions to XPS are withdrawn. The insertion of P in the g-C_3N_4 takes place by replacing C positions, either at bay or corner sites [68], including also the formation of P-O bindings, ascribed to the presence of hydroxyl groups.

Elemental analysis was carried out to compare the N/C ratios before and after doping with P, see results in Table 1. The unmodified CN displayed a value N/C= 1.485 (at.) which is close to the theoretical value of N/C= 4/3 expected for g-C_3N_4. The doping with P led to an increase in this ratio: 1.499 (P-CN-2%), 1.505 (P-CN-4%), 1.600 (P-CN-8%), and 1.574 (P-CN-12%). This tendency provides alternative evidence of a partial replacement of C by P. From bare CN to P-CN-8%, it is observed an increase of N/C ratio, with a waned value describing a minimum before further rise of P doping as observed with P-CN-12%. This replacement can be attributed, especially at low concentrations of P, to the substitution of corner or bay C positions as already reported in the literature with similar materials [61].
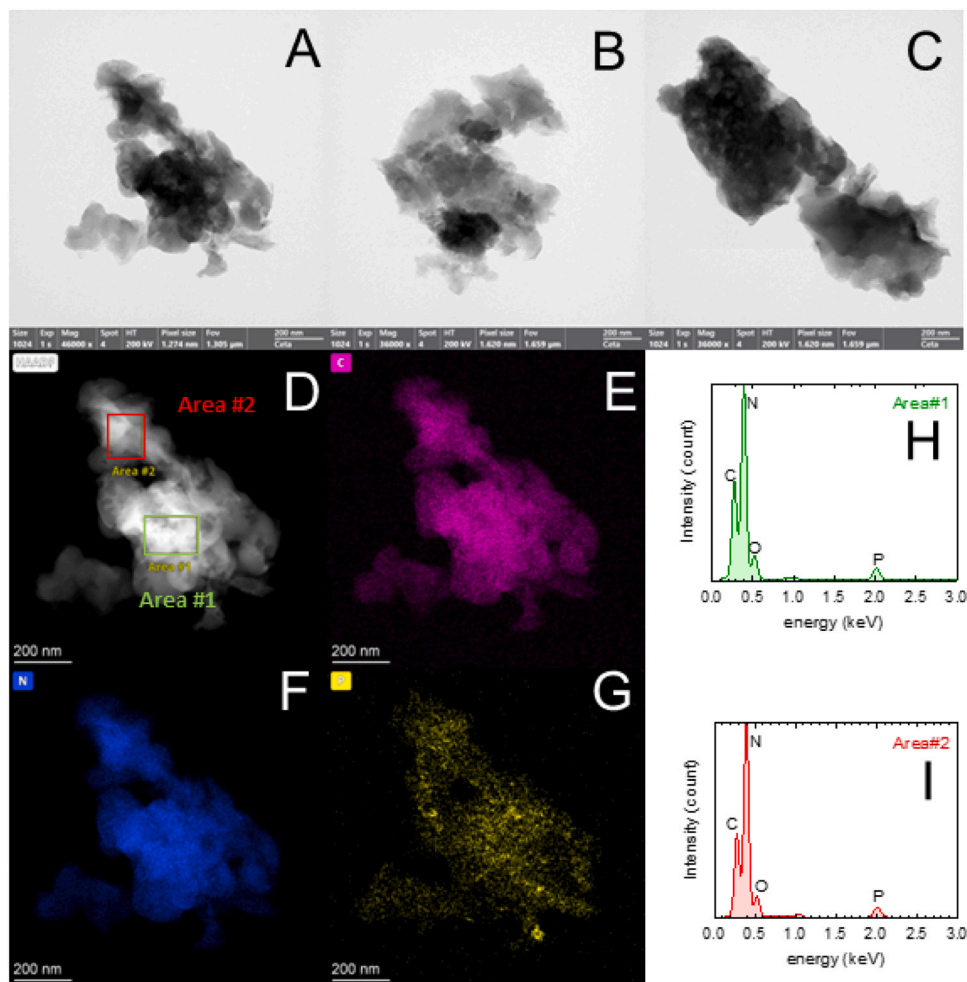

Fig. 6. HR-STEM micrographs and EDX analysis of P-CN-4% sample. TEM images (A-B), HAADF image (D) and their element mapping of C (E), N (F) and P (G), and EDX spectra of two selected areas of HAADF image (D).

In summary, according to the global results of FTIR, XPS, and elemental analysis, it can be hypothesized that P is exchanged by C atoms in the graphitic structure [61]. Two points of attack have been reported in the literature, i.e. bay and corner carbon [80,81]. Moreover, phosphate can also be linked to N atoms, i.e. at the edge or building a bridge [69]. Among all these possibilities, the substitution of C seems to be preferential, although the positions at margins and defects of the CN structure are also plausible as phosphoramide or phosphorimide moieties [61].

The morphology and distribution of P were observed by STEM technique coupled with EDX analysis. Fig. 6 depicts some pictures of the P-CN-4% samples. The images show the presence of laminar particles that can be aggregated in bigger associations of up to 500 nm. EDX microanalysis led to the elements imaging, i.e. C, N, and P. The EDX spectra of two selected areas are also provided, recording the existence of P in the sample. The mapping images showed random and almost uniform distribution of P dispersion. It should be noticed that the intensity of P mapping was much lesser intense than the corresponding for C and N due to the low content of P onto P-CN-4%, i.e. roughly 4%.

The optical properties were assessed by DRS-UV–visible. Fig. 7A depicts the absorption spectra of the samples. Moreover, the spectra of the emitted radiation by the lamps is also included. In general terms, an intensive absorption enhancement in the UV and visible light regions is observed after P doping, and the band gap was narrowed as the P precursor amount was raised. The bare CN displayed a strong decay of absorbance after 420 nm and a bandgap value (see Fig. 7B) of roughly 2.7 eV. The P-doping enhanced the absorbance in the visible region with a partial red-shifted of the absorption spectra and conferred to the material a characteristic brownish color [82]. The P-CN samples showed an important decrease in the absorbance at 420 nm, which diminished the rate of the absorbance decay afterward. This enables the material to absorb in the visible region, which is very limited for CN, enlarged as the amount of the doping P was increased. This extended absorbance up to 800 nm has been previously reported in the literature using different P precursor and synthesis strategies, such as phosphoric acid [82], phosphonic acid [82], hexachloro-tricyclophosphazene [69], or natural P sources like phytic acid [81]. Moreover, the bandgap was narrowed from 2.7 eV of bare CN to 2.5 eV (P-CN-4%) and 2.0 eV (P-CN-12%). Previous works have reported similar behavior by P tuning of g-C$_3$N$_4$, further confirmed by DFT calculations [83]. The reason for the red-shifted absorption edge has been attributed to the 3p stated of P located at the bottom of the conduction band in the g-C$_3$N$_4$, which contributes to a stabilization of the conduction band in lower energies and therefore a decrease of the bandgap [84–86].

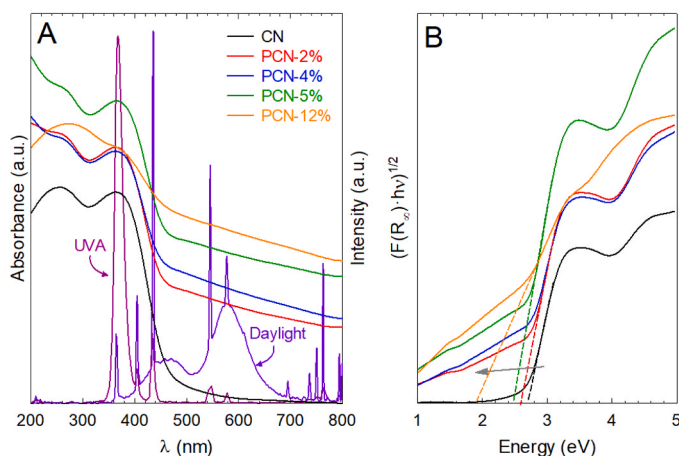Fig. 8 illustrates the photoluminescence (PL) spectra of the samples

Fig. 7. UV–visible absorption spectra of the P-CN samples and the emitting radiation spectra of the UVA and daylight lamps used (A) and bandgap determination of P-CN samples (B).
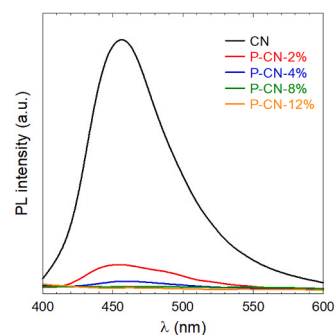

Fig. 8. Photoluminescence spectra of P-CN samples.

after excitation at 365 nm, the wavelength of the radiation used in the photocatalytic tests. The intensity of the PL peak can be associated with the recombination rate of the photogenerated charges, an undesirable effect for the photocatalytic process. A low-intensity PL signal implies a lower recombination rate of photoinduced electrons and holes; that means, a higher photocatalytic activity [87]. The PL spectrum of undoped CN shows a peak with a maximum centered at 458 nm. The PL spectra of the doped samples show that the doping of the P in the graphitic carbon nitride led to a dramatic decrease in the PL peak. Doping doses over 4% of P were conducted to negligible PL response, providing evidence of efficient separation of charges due to the presence of defects in the structure after doping, restraining the recombination rate of electron-hole pairs after P-doping. This effect has also been reported in previous works [82,88,89] and ascribed to the promoted electron delocalization on surface terminal sites after doping and structural advantages of P-CN, such as the interconnected nanosheets, as deduced from the higher crystal size, that can greatly curtail the charge migration [69].

3.2. Photocatalytic production of cinnamaldehyde with the P-CN samples

The photocatalytic activity of P-CN samples was assessed for the reaction of oxidation of cinnamyl alcohol (CA) to cinnamaldehyde (CD). The temporal evolution of the normalized CA concentration and the yield of CD production are depicted in Fig. 9A. The pseudo-first order rate constant of CA abatement (k_{CA}) is available in Fig. 9B and Fig. 9C depicts the conversion after 5 h of reaction and the average selectivity to CD. The use of bare CN led to 37% of CA oxidation, with a selectivity of ~10%. The modification with P of the carbon nitride improved the photocatalytic oxidation of CA at low P doping dosage, i.e. P-CN-2%. However, at excessively high P doping (P-CN-12%) the kinetics of CA oxidation was worse than the non-doped sample, as the estimated k_{CA} and the conversion values at 5 h show. However, in terms of selectivity to CD, the presence of P improved the selectivity if compared to the bare CN in all the cases. It was observed a maximum selectivity with P-CN-4% (S_{CD}=49%). Table 2 summarizes the main kinetic parameters for all the tested samples. The quantum efficiency was calculated from the LVRPA estimation and the initial rate of cinnamyl alcohol abatement. The order of radiation uptake is, following the photocatalytic activity, P-CN-2% > P-CN-4% > CN > P-CN-8% > P-CN-12%. It corroborates the tendency observed for k_{CA}. Additionally, a test in the presence of visible radiation (>400 nm) instead of UVA (365 nm) was conducted. The sample P-CN-4% showed less activity under visible radiation. As shown in Table 2, the k_{CA} under visible illumination was only 39% of the achieved under UVA. The results indicate lower photocatalytic activity under visible radiation, which follows the absorptivity trend of P-CN-4%. However, due to the incorporation of P in the structure and the red-shifted absorption spectra, the samples performed certain activity under the visible region.

The use of organic solvents has been widely researched to raise the selectivity of the process [90], even to the detriment of the conversion of the parent alcohol. Acetonitrile is one of the most studied organic
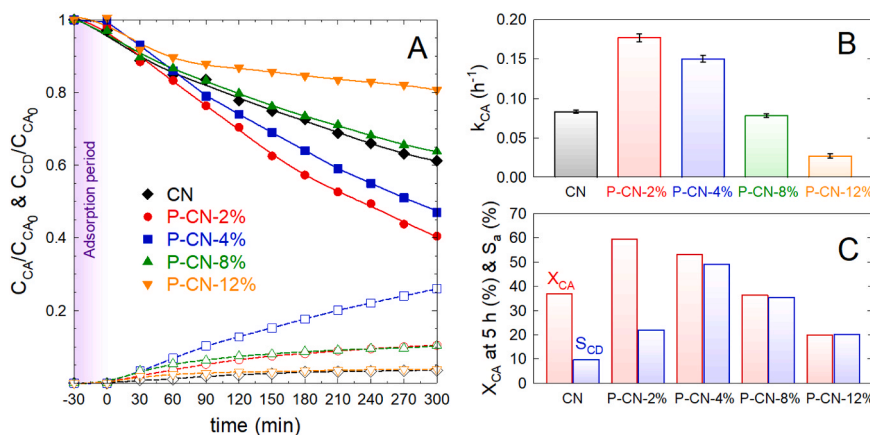
Fig. 9. Photocatalytic oxidation of cinnamyl alcohol (CA) to cinnamaldehyde (CD). (A) Temporal evolution of the normalized concentration of CA and CD yield. (B) Pseudo-first order rate constant of CA abatement. (C) CA conversion at 5 h and average selectivity to CD. *Experimental conditions: UVA radiation; V= 350 mL; C_{CA}= 1 mM; $C_{catalyst}$= 0.5 g L^{-1}, T = 20 °C.*

Table 2
Kinetic parameters of the photocatalytic production of cinnamaldehyde with P-CN samples under UVA and visible radiation.

Sample	$r_{CA,0} \cdot 10^3$ (mM min^{-1})	$e^{\alpha,\nu} \cdot 10^8$ (Einstein $cm^{-3} s^{-1}$)	Q_E (%)	k_{CA} (h^{-1})	X_{CA} at 5 h (%)	S_{CD} (%)
UVA (365 nm)						
CN	1.383	1.620	0.142	0.083	36.9	9.8
P-CN-2%	2.950	1.944	0.253	0.177	59.6	22.0
P-CN-4%	2.500	2.025	0.206	0.150	53.0	49.2
P-CN-8%	1.300	2.349	0.092	0.078	36.3	35.3
P-CN-12%	0.450	2.268	0.033	0.027	19.8	20.2
Visible (>400 nm)						
P-CN-4%	0.985	-	-	0.059	25.5	16.1

solvents since it raises the selectivity of cinnamaldehyde formation in the absence of water [91]. To compare the benefits of P doping over g-C$_3$N$_4$, the performance of the non-doped CN and the sample P-CN-4%,
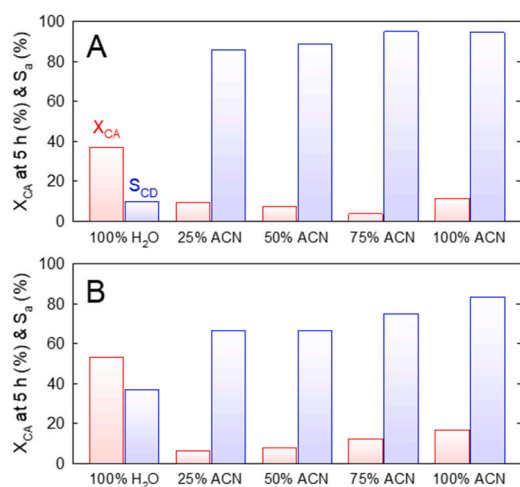

Fig. 10. Conversion of cinnamyl alcohol (CA) and cinnamaldehyde (CD) selectivity in water-acetonitrile (ACN) mixtures with CN (A) and P-CN-4% (B) samples. *Experimental conditions: UVA radiation; V= 350 mL; C_{CA}= 1 mM; $C_{catalyst}$= 0.5 g L^{-1}, T = 20 °C.*

which displayed the highest CD yield, were further investigated in water-acetonitrile mixtures. Fig. 10 illustrates the conversion after 5 h of reaction and the average selectivity of CD formation for both catalysts at different water-acetonitrile proportions. It can be observed that an important decrease in the conversion is observed when adding acetonitrile. However, the reaction becomes more selective to CD formation, probably due to the suppression of hydroxyl radical contribution which is more unselective than others such as superoxide. Moreover, when comparing the CN and P-CN-4% samples, it can be stated a lesser selectivity in the presence of acetonitrile for P-CN-4%. The presence of phosphate groups on the surface contributes to a higher surface-HO presence that might interact with CD during oxidation, which could explain the lesser selectivity achieved if compared to bare CN.

3.3. Photocatalytic mechanism and degradation pathway with P-CN-4%

The impact of the reactive oxidation species (ROS) involved in the photocatalytic oxidation of cinnamyl alcohol over P-CN-4% was tentatively studied by the addition of chemical radical scavengers [35], as shown in Fig. 11. It should be noted that the interaction of the chemical scavengers in the photocatalytic mechanism is not completely selective and should be analyzed with caution [36,37].

Firstly, the role played by the hydroxyl radical was assessed by adding to the solution tert-butyl alcohol (TBA), due to the high reactivity of TBA with HO$^\bullet$ ($k_{TBA,HO\bullet}$=6.2 × 10^8 M^{-1} s^{-1}) [92]. In the presence of TBA, the CA profile was slowed down, although the reaction was not completely stopped. The hydroxyl radical has been reported as an unselective oxidant species, and in the case of cinnamyl alcohol, the attack of HO to the C=C of the alkyl chain releases benzaldehyde or acetaldehyde as undesirable byproducts [93,94]. The role played by HO$^\bullet$ in the degradation mechanism of P-CN-4% activation and CA oxidation was further analyzed by the use of 2-HO-TPA as an indirect molecule probe of HO$^\bullet$ existence. It is well known that TPA can trap HO$^\bullet$ selectively leading to the formation of the fluorescent 2-HO-TPA [38]. Fig. 11 depicts the temporal evolution of 2-OH-TPA during the photocatalytic transformation of TPA in the presence of P-CN-4%. As illustrated in the spectra recorded (Fig. 11C), the spectra are barely defined, being appreciated as an important signal-to-noise ratio that manifests the low production of HO$^\bullet$. This fact was further corroborated by the determination of the temporal evolution of the concentration of 2-OH-TPA, see Fig. 11D. From this figure, it is observed that a plateau is reached after 30–60 min. Noteworthy, the values obtained for the concentration of the generated 2-OH-TPA are below the limit of detection. This poor formation of the fluorescent 2-OH-TPA provides evidence of negligible production of HO$^\bullet$, whose impact according to the scavengers' tests was
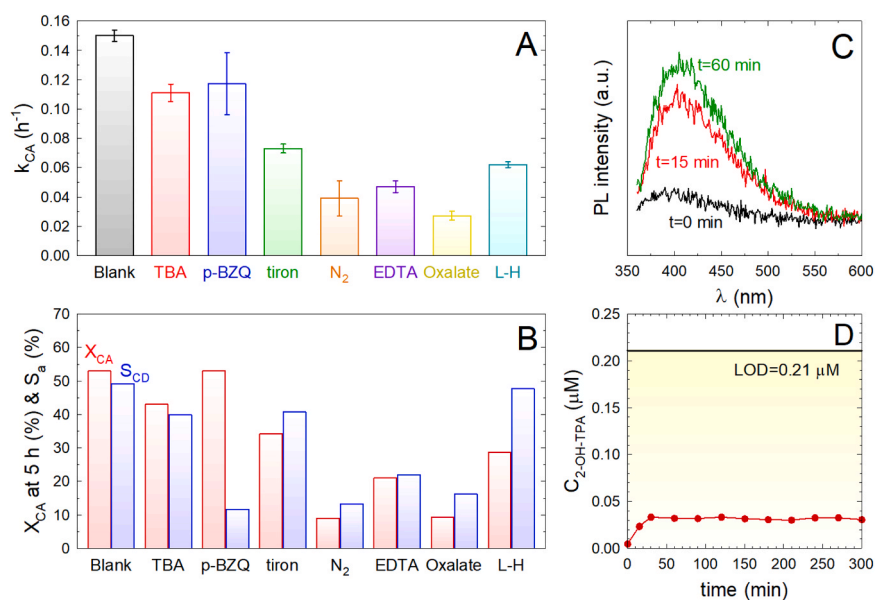
Fig. 11. Photocatalytic oxidation of cinnamyl alcohol (CA) to cinnamaldehyde (CD). (A) The pseudo-first order rate constant of CA abatement with P-CN-4% in the presence of chemical scavengers (A) and the CA conversion at 5 h and average selectivity to CD (B). (Photoluminescence spectra of 2-OH-TPA (C) and temporal evolution of the concentration of 2-OH-TPA (D) during the photocatalytic transformation of TPA with P-CN-4%. *Experimental conditions: UVA radiation; V= 350 mL; C_{CA}= 1 mM; $C_{catalyst}$= 0.5 g L^{-1}; $C_{scavenger}$= 10 mM; C_{TPA}= 1 mM; T = 20 °C.*

suggested to be minimal. According to the reported band alignment for g-C$_3$N$_4$, the redox potential of the valence band does not display enough potential to trigger the oxidation of water molecules to HO$^\bullet$ [14,95].

Secondly, the role played by the superoxide radical was assessed by adding -p-benzoquinone (p-BZQ), tiron, or removing the dissolved O$_2$ bubbling N$_2$ instead of air [96]. The use of p-BZQ is widely extended to check the role played by superoxide radicals in photocatalysis tests [35], due to the high reactivity ($k_{p-BZQ,O2\bullet}$ =10^9 M^{-1} s^{-1} [97]). However, some authors have recently warned about the complexity of p-BZQ in aqueous photocatalytic media [36,37]. For instance, p-BZQ can trap electrons ($k_{p-BZQ,e-}$=1.35 × 10^9 M^{-1} s^{-1}[98]) leading to the formation of semiquinone radicals [37], it displays also a high reactivity with HO$^\bullet$ ($k_{p-BZQ,HO\bullet}$=6.6 × 10^9 M^{-1} s^{-1} [99]), p-BZQ is also photolyzed giving rise to extra O$_2^{\bullet-}$ [100], or being photo-activated to release single oxygen (^{1}O$_2$) [101]. To overcome these drawbacks, tiron, which is commonly used to test the presence of O$_2^{\bullet-}$ [36], was selected for additional analysis, although it also may react with HO$^\bullet$ (k_{tiron}=10^9 M^{-1} s^{-1} [102]). In the presence of p-BZQ, no significant alteration of the kinetics was observed if compared to the blank, and the selectivity was dramatically diminished; however, tiron did lead to a ~50% depletion of k_{CA} with no so huge affectation to the selectivity. Bearing in mind the lack of HO$^\bullet$ participation, the decrease in the presence of tiron may be taken as proof of O$_2^{\bullet-}$ participation. Additionally, a test under N$_2$ displacement of dissolved O$_2$ was conducted. It has been reported that an atmosphere of pure O$_2$ has led to boosted conversion but very similar selectivity if compared to air, Ar, or N$_2$ [103]. In this case, an abrupt decrease in the kinetics of CA oxidation was observed, which may suggest a high importance of O$_2^{\bullet-}$ in the oxidative process of CA. Nonetheless, it should be also considered that in the absence of any electron acceptor such as O$_2$, the recombination effect is potentiated, rising as conclusion an overrated participation of O$_2^{\bullet-}$. The results attained with tiron and N$_2$, cautiously considered, may provide evidence about the relevance of O$_2^{\bullet-}$ in the process if compared to other ROS.

Thirdly, the importance of the photo-generated holes was studied by adding oxalic acid [104] as oxalate anions can be easily oxidized by the holes to produce CO$_2$. Oxalate anion also can trap HO$^\bullet$; however, the kinetics is slow ($k_{Oxalate,HO\bullet}$= 1.5 × 10^7 M^{-1} s^{-1} [105]), and the production of HO$^\bullet$ has been discharged in P-CN-4%. In the presence of oxalic acid, the kinetic of CA oxidation was negatively influenced,

suggesting the importance of photo-generated holes in the process. For further corroboration, EDTA was also tested as a hole scavenger. EDTA has been reported as a superior scavenger to oxalic acid due to its strong chelating effect and ability to directly fill electrons into the valance band [106]. The results attained with EDTA confirm the importance of the hole in the CA oxidation.

Finally, the plausible participation of singlet oxygen (^{1}O$_2$) was verified by a test adding L-Histidine (L-H). L-H has a great ability to react with ^{1}O$_2$ and HO$^\bullet$ ($k_{L-H,HO\bullet}$= 1.5 × 10^7 M^{-1} s^{-1} [35]). As the production of HO$^\bullet$, the 60% decrease in k_{CA} may be attributed to the participation of ^{1}O$_2$.

The mechanism of oxidation of cinnamyl alcohol involves the photogenerated holes by the formation of an intermediate organic radical that could be further oxidized to the aldehyde by the holes [107] or by the superoxide radicals [96]. This mechanism would explain the results achieved in this work, in which the participation was tentatively identified as h$^+$ > O$_2^{\bullet-}$ ~ ^{1}O$_2$.

A tentative proposal of the band alignment was carried out as an approach from the estimation of the valence band by XPS and the bandgap obtained from the Tauc plot of the absorption data of DRS-UV–visible [73,76,79]. Fig. 12A depicts the valence band edge obtained from XPS, leading to a slight shift to a higher potential value after P-doping, i.e. the redox potential of the holes are 1.10 and 1.26 V for CN and P-CN-4%, respectively. After considering the bandgap values, a scheme of the bands' placement is depicted in Fig. 12B, where it is stated the unfeasibility of formation of hydroxyl radical from the oxidation of water, redox of the pair H$_2$O/HO$^\bullet$, + 2.31 V [108]. On the contrary, the formation of O$_2^{\bullet-}$ is favorable, redox O$_2$/O$_2^{\bullet-}$, − 0.33 V [109]. A comparison between CN and P-CN-4% reveals that no substantial changes in the band's alignment occur, so the better performance of P-CN-4% relies on the higher migration of charges due to the presence of P defects that minimize the recombination effect.

The products generated during the photocatalytic oxidation of cinnamyl alcohol were identified by liquid chromatography coupled to electrospray ionization under positive mode and mass spectrometry with a quadrupole time-of-flight, LC-ESI(+)-QTOF, using the photocatalyst with the best performance, i.e. P-CN-4%. Both, positive and negative ionization modes were tested, restricting the study under positive mode since cinnamyl alcohol and aldehyde were prone to it.
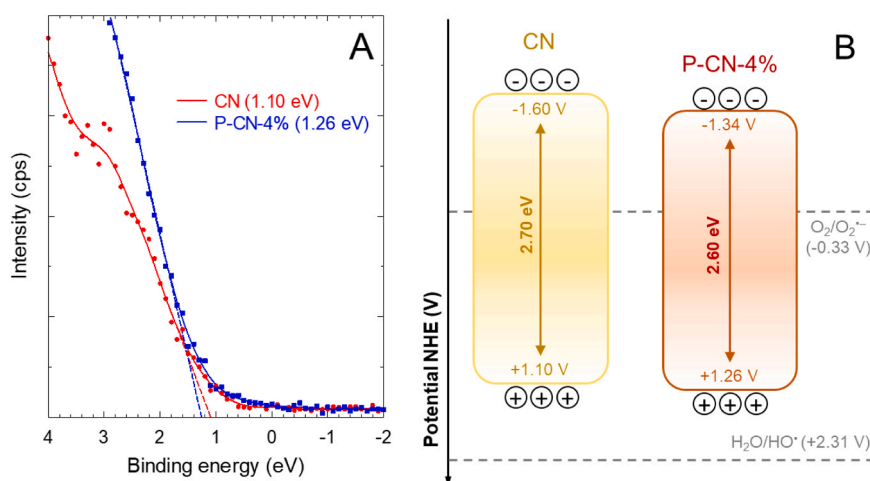
Fig. 12. Determination of the valence band edge of CN and P-CN-4% by XPS (A) and bands alignment proposal (B).

Cinnamyl alcohol is an allyl alcohol, whose ionization under positive mode led to the loss of H₂O, [M-H₂O]⁺=117.06054. The detected reaction byproducts and a plausible degradation pathway is depicted in Fig. 13. The aerobic oxidation of cinnamyl alcohol has been reported to occur spontaneously under the presence of oxygen and daylight radiation, appreciating the degradation after a long time though, i.e. 54 weeks [110]. Under these circumstances, the oxidation of CA can take place on the allyl alcohol group, leading to the formation of cinnamaldehyde (CD); alternatively, triggering an epoxy ring if the oxidation attack goes through the unsaturation of the allyl chain, generating the epoxy-cinnamyl alcohol (epoxy-CA). Both routes have been observed during the photocatalytic activation of P-CN-4%; nonetheless, the CD appeared in much more intensity in the extracted ion chromatograms if compared to epoxy-CA, which suggests a great preference for the oxidation of the terminal alcohol, preserving the double bond of the chain. Studies of photocatalytic transformation of CA over TiO₂-based catalysts have concluded that the pathway route addresses the formation of CD and benzaldehyde as the main degradation byproducts [111,112]. Other catalytic oxidation systems involving the activation of hydrogen peroxide over catalysts based on iron or palladium as active species have described appreciable contribution of epoxide formation, either in the cinnamyl alcohol or aldehyde formulas [113]. Under the action of

P-CN-4%, the further oxidation of CD led to the generation of cinnamic acid (CC), which appeared in similar intensity levels as CD, which is consistent with the other studies under the presence of oxygen [110–112]. The subsequent oxidation of CC led to the formation of phenylacetaldehyde [111], detected at long reaction times, i.e. 5 h. Alternatively, a [M-H]⁺=167.0703 no reported previously was registered in this work, which according to in silico oxidation prediction tools [114], corresponds to hydroxylation of the allyl bond of cinnamic acid. However, these two byproducts produced from CC appeared at an intensity of one magnitude order below CC, which as the epoxy derivatives led to mass errors in ppm higher than the major compounds. No further oxidation to lower transformation products was detected, being the release of CD and CC, the most appreciable products detected in the photo-oxidation of CA.

4. Conclusions

The incorporation of P into graphitic carbon nitride with sodium phosphate in a two-step synthesis process has been successfully carried out. The crystalline structure suggested that P was incorporated in the external faces of the plates or the heptazine rings, attacking the layered structure. The FTIR analysis pointed out the decrease of vibration of the
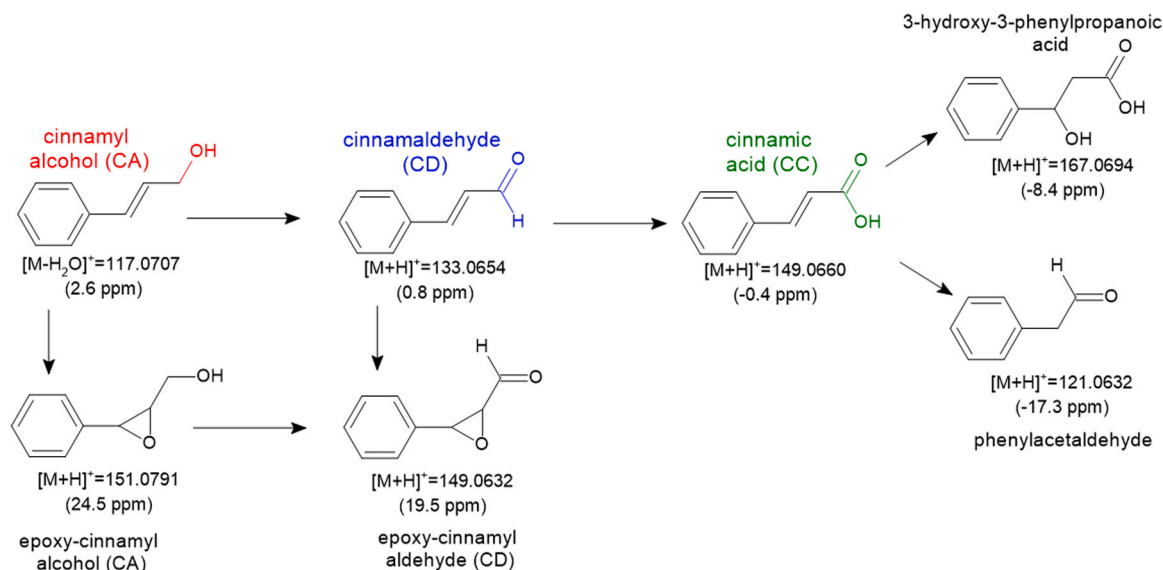

Fig. 13. Proposed degradation mechanism of cinnamyl alcohol over P-CN-4%.

terminal –NH$_x$ groups and the appearance of a P-N bond anchoring of phosphate groups to N atoms. This fact was further confirmed by XPS analysis, deducing a plausible attack of phosphate to C positions, leading to the formation of terminal phosphate groups linked to N. The P is expected to be by C atoms in the graphitic structure at two points, i.e. bay and corner carbon, as NMR analysis suggested. Moreover, phosphate can also be linked to N atoms, i.e. at the edge or building a bridge. Regarding the optical properties, an intensive absorption enhancement in the UV and visible light regions was observed after P doping, and the band gap was narrowed as the P precursor amount was raised, from 2.7 (bare graphitic carbon) to 2.6 eV (sample doped with 4%). The photoluminescence properties of the doped samples showed a dramatic decrease in the PL peak. Doses over 4% of P were subjected to negligible PL response, providing evidence of efficient separation of charges due to the presence of defects in the structure after doping.

The P doping modified the photocatalytic activity of the oxidation reaction of cinnamyl alcohol (CA) to cinnamaldehyde (CD). Although the modification with P improved the photocatalytic oxidation of CA, it was only achieved at low P doping dosage, i.e. P-CN-2%, the selectivity to CD in the presence of P was improved if compared to the bare CN in all the cases, reaching a maximum of ~50% (P-CN-4%). The influence of the solvent was also studied by carrying out tests on acetonitrile. The presence of acetonitrile led to a rise of the selectivity to the detriment of lower conversion of the alcohol. The bare CN sample led to almost 100% of selectivity in acetonitrile while the P-CN-4% sample only led to 80%. Finally, the relative influence of the reactive oxygen species involved in the process of photocatalytic oxidation in water was studied. The mechanism of oxidation of cinnamyl alcohol involves the photogenerated holes by the formation of an intermediate organic radical that could be further oxidized to the aldehyde by the holes or by the superoxide radicals, with a negligible contribution of the hydroxyl radicals. The analysis of the transformation products provides evidence of a preferential oxidation route of the alcohol group, triggering the oxidation to cinnamaldehyde and subsequent release of cinnamic acid.

CRediT authorship contribution statement

Rafael Rodríguez Solís: Data curation, Formal analysis, Funding acquisition, Supervision, Validation, Writing – original draft, Writing – review & editing, Project administration. **Mario J. Muñoz-Batista:** Conceptualization, Formal analysis, Funding acquisition, Project administration, Supervision, Writing – review & editing. **Mónica Calero:** Formal analysis, Resources, Supervision, Validation, Writing – review & editing. **María Ángeles Martín-Lara:** Formal analysis, Supervision, Validation, Writing – review & editing. **Alba Picón:** Investigation. **María Alejandra Quintana:** Investigation, Methodology.

Declaration of Competing Interest

The authors declare that they have no known competing financial interests or personal relationships that could have appeared to influence the work reported in this paper.

Data availability

Data will be made available on request.

Acknowledgements

References

[1] J. Cocchiara, C.S. Letizia, J. Lalko, A. Lapczynski, A.M. Api, Fragrance material review on cinnamaldehyde, Food Chem. Toxicol. 43 (2005) 867–923, https://doi.org/10.1016/J.FCT.2004.09.014.

[2] M. Friedman, N. Kozukue, L.A. Harden, Cinnamaldehyde content in foods determined by gas chromatography-mass spectrometry, J. Agric. Food Chem. 48 (2000) 5702–5709, https://doi.org/10.1021/JF000585G.

[3] C.M. Franz, K.H.C. Baser, I. Hahn-Ramssl, Herbs and aromatic plants as feed additives: Aspects of composition, safety, and registration rules. in: Feed Additives: Aromatic Plants and Herbs in Animal Nutrition and Health, Academic Press, 2020, pp. 35–56, https://doi.org/10.1016/B978-0-12-814700-9.00003-0.

[4] A.A. Doyle, J.C. Stephens, A review of cinnamaldehyde and its derivatives as antibacterial agents, Fitoterapia 139 (2019) 104405, https://doi.org/10.1016/J.FITOTE.2019.104405.

[5] L. Lu, C. Shu, L. Chen, Y. Yang, S. Ma, K. Zhu, B. Shi, Insecticidal activity and mechanism of cinnamaldehyde in C. elegans, Fitoterapia 146 (2020) 104687, https://doi.org/10.1016/J.FITOTE.2020.104687.

[6] J.D. Grunwaldt, C. Keresszegi, T. Mallat, A. Baiker, In situ EXAFS study of Pd/Al$_2$O$_3$ during aerobic oxidation of cinnamyl alcohol in an organic solvent, J. Catal. 213 (2003) 291–295, https://doi.org/10.1016/S0021-9517(02)00083-0.

[7] T. Mallat, Z. Bodnar, P. Hug, A. Baiker, Selective oxidation of cinnamyl alcohol to cinnamaldehyde with air over Bi-Pt/alumina catalysts, J. Catal. 153 (1995) 131–143, https://doi.org/10.1006/JCAT.1995.1115.

[8] R.F.M. Frade, D. Simão, C.A.M. Afonso, Isolation of cinnamaldehyde from cinnamon, in: in: Comprehensive Organic Chemistry Experiments for the Laboratory Classroom, The Royal Society of Chemistry, 2016, pp. 23–25, https://doi.org/10.1039/9781849739634-00023.

[9] R. Wang, R. Wang, B. Yang, Comparison of volatile compound of cinnamon (Cinnamomum cassia Presl) bark prepraed by hydrodistillation and headspace solid phase microextraction, J. Food Process Eng. 34 (2011) 175–185, https://doi.org/10.1111/J.1745-4530.2008.00347.X.

[10] F.A. Al-Bayati, M.J. Mohammed, Isolation, identification, and purification of cinnamaldehyde from Cinnamomum zeylanicum bark oil. An antibacterial study, Pharm. Biol. 47 (2009) 61–66, https://doi.org/10.1080/13880200802430607.

[11] P.I. Modi, J.K. Parikh, M.A. Desai, Intensified approach towards isolation of cinnamon oil using microwave radiation: parametric, optimization and comparative studies, Ind. Crops Prod. 173 (2021) 114088, https://doi.org/10.1016/J.INDCROP.2021.114088.

[12] P.I. Modi, J.K. Parikh, M.A. Desai, Sonohydrodistillation: innovative approach for isolation of essential oil from the bark of cinnamon, Ind. Crops Prod. 142 (2019) 111838, https://doi.org/10.1016/J.INDCROP.2019.111838.

[13] Q. Fan, F. Huang, L. Zhou, W. He, X. Jiang, Z. Na, P. Gongpan, H. Hu, Q. Song, Development of a strategy for a quick process for separation of volatile compounds in counter-current chromatography: purification of cinnamaldehyde from Cinnamomum cassia by high performance counter-current chromatography, Prep. Biochem Biotechnol. 51 (2021) 1056–1059, https://doi.org/10.1080/10826068.2021.1894444.

[14] G. Marcì, E.I. García-López, L. Palmisano, Polymeric carbon nitride (C$_3$N$_4$) as heterogeneous photocatalyst for selective oxidation of alcohols to aldehydes, Catal. Today 315 (2018) 126–137, https://doi.org/10.1016/J.CATTOD.2018.03.038.

[15] L. Chen, J. Tang, L.N. Song, P. Chen, J. He, C.T. Au, S.F. Yin, Heterogeneous photocatalysis for selective oxidation of alcohols and hydrocarbons, Appl. Catal. B 242 (2019) 379–388, https://doi.org/10.1016/J.APCATB.2018.10.025.

[16] Z. Shen, Y. Hu, B. Li, Y. Zou, S. Li, G. Wilma Busser, X. Wang, G. Zhao, M. Muhler, State-of-the-art progress in the selective photo-oxidation of alcohols, J. Energy Chem. 62 (2021) 338–350, https://doi.org/10.1016/J.JECHEM.2021.03.033.

[17] L. Xiong, J. Tang, Strategies and challenges on selectivity of photocatalytic oxidation of organic substances, Adv. Energy Mater. 11 (2021) 2003216, https://doi.org/10.1002/AENM.202003216.

[18] S. Hazra, E. Malik, A. Nair, V. Tiwari, P. Dolui, A.J. Elias, Catalytic oxidation of alcohols and amines to value-added chemicals using water as the solvent, Chem. Asian J. 15 (2020) 1916–1936, https://doi.org/10.1002/ASIA.202000299.

[19] Y. Wang, X. Wang, M. Antonietti, Polymeric graphitic carbon nitride as a heterogeneous organocatalyst: from photochemistry to multipurpose catalysis to sustainable chemistry, Angew. Chem. 51 (2012) 68–89, https://doi.org/10.1002/ANIE.201101182.

[20] W. Zhang, A. Bariotaki, I. Smonou, F. Hollmann, Visible-light-driven photooxidation of alcohols using surface-doped graphitic carbon nitride, Green Chem. 19 (2017) 2096–2100, https://doi.org/10.1039/C7GC00539C.

[21] A. Akhundi, A. Badiei, G.M. Ziarani, A. Habibi-Yangjeh, M.J. Muñoz-Batista, R. Luque, Graphitic carbon nitride-based photocatalysts: toward efficient organic transformation for value-added chemicals production, Mol. Catal. 488 (2020) 110902, https://doi.org/10.1016/J.MCAT.2020.110902.

[22] M. Bellardita, E.I. García-López, G. Marcì, I. Krivtsov, J.R. García, L. Palmisano, Selective photocatalytic oxidation of aromatic alcohols in water by using P-doped g-C$_3$N$_4$, Appl. Catal. B 220 (2018) 222–233, https://doi.org/10.1016/J.APCATB.2017.08.033.

[23] A. Bagherzade, F. Nemati, H.T. Nahzomi, Computational and experimental evidence of Pd supported P-doped porous graphitic carbon nitride as a highly efficient and exceptionally durable photocatalyst for boosted visible-light-driven

benzyl alcohol oxidation, J. Phys. Chem. Solids 152 (2021) 109985, https://doi.org/10.1016/J.JPCS.2021.109985.

[24] S. Cao, Q. Huang, B. Zhu, J. Yu, Trace-level phosphorus and sodium co-doping of g-C$_3$N$_4$ for enhanced photocatalytic H$_2$ production, J. Power Sources 351 (2017) 151–159, https://doi.org/10.1016/J.JPOWSOUR.2017.03.089.

[25] A. Altomare, N. Corriero, C. Cuocci, A. Falcicchio, A. Moliterni, R. Rizzi, QUALX2.0: a qualitative phase analysis software using the freely available database POW_COD, J. Appl. Crystallogr 48 (2015) 598–603, https://doi.org/10.1107/S1600576715002319.

[26] Á. Pérez-Molina, L.M. Pastrana-Martínez, S. Morales-Torres, F.J. Maldonado-Hódar, Photodegradation of cytostatic drugs by g-C$_3$N$_4$: synthesis, properties and performance fitted by selecting the appropriate precursor, Catal. Today 418 (2023) 114068, https://doi.org/10.1016/J.CATTOD.2023.114068.

[27] P. Makuła, M. Pacia, W. Macyk, How to correctly determine the band gap energy of modified semiconductor photocatalysts based on UV–vis spectra, J. Phys. Chem. Lett. 9 (2018) 6814–6817, https://doi.org/10.1021/acs.jpclett.8b02892.

[28] S. Landi, I.R. Segundo, E. Freitas, M. Vasilevskiy, J. Carneiro, C.J. Tavares, Use and misuse of the Kubelka-Munk function to obtain the band gap energy from diffuse reflectance measurements, Solid State Commun. 341 (2022) 114573, https://doi.org/10.1016/J.SSC.2021.114573.

[29] R.R. Solís, M.A. Quintana, M.Á. Martín-Lara, A. Pérez, M. Calero, M.J. Muñoz-Batista, Boosted activity of g-C$_3$N$_4$/UiO-66-NH$_2$ heterostructures for the photocatalytic degradation of contaminants in water, Int. J. Mol. Sci. 23 (2022) 12871, https://doi.org/10.3390/IJMS232112871/S1.

[30] N. Serpone, Relative photonic efficiencies and quantum yields in heterogeneous photocatalysis, J. Photochem. Photobiol. A Chem. 104 (1997) 1–12, https://doi.org/10.1016/S1010-6030(96)04538-8.

[31] G. Li Puma, A. Brucato, Dimensionless analysis of slurry photocatalytic reactors using two-flux and six-flux radiation absorption–scattering models, Catal. Today 122 (2007) 78–90, https://doi.org/10.1016/J.CATTOD.2007.01.027.

[32] O.M. Alfano, D. Bahnemann, A.E. Cassano, R. Dillert, R. Goslich, Photocatalysis in water environments using artificial and solar light, Catal. Today 58 (2000) 199–230, https://doi.org/10.1016/S0920-5861(00)00252-2.

[33] M.J. Muñoz-Batista, A. Kubacka, O. Fontelles-Carceller, D. Tudela, M. Fernández-García, Surface CuO, Bi$_2$O$_3$, and CeO$_2$ species supported in TiO$_2$-anatase: study of interface effects in toluene photodegradation quantum efficiency, ACS Appl. Mater. Interfaces 8 (2016) 13934–13945, https://doi.org/10.1021/ACSAMI.6B03081.

[34] M.A. Quintana, R.R. Solís, M. Ángeles Martín-Lara, G. Blázquez, F. Mónica Calero, M.J. Muñoz-Batista, Enhanced boron modified graphitic carbon nitride for the selective photocatalytic production of benzaldehyde, Sep Purif. Technol. 298 (2022) 121613, https://doi.org/10.1016/J.SEPPUR.2022.121613.

[35] M. Pelaez, P. Falaras, V. Likodimos, K. O'Shea, A.A. de la Cruz, P.S.M. Dunlop, J. A. Byrne, D.D. Dionysiou, Use of selected scavengers for the determination of NF-TiO$_2$ reactive oxygen species during the degradation of microcystin-LR under visible light irradiation, J. Mol. Catal. A Chem. 425 (2016) 183–189, https://doi.org/10.1016/j.molcata.2016.09.035.

[36] E.M. Rodríguez, G. Márquez, M. Tena, P.M. Álvarez, F.J. Beltrán, Determination of main species involved in the first steps of TiO$_2$ photocatalytic degradation of organics with the use of scavengers: the case of ofloxacin, Appl. Catal. B 178 (2015) 44–53, https://doi.org/10.1016/j.apcatb.2014.11.002.

[37] J.T. Schneider, D.S. Firak, R.R. Ribeiro, P. Peralta-Zamora, Use of scavenger agents in heterogeneous photocatalysis: truths, half-truths, and misinterpretations, Phys. Chem. Chem. Phys. 22 (2020) 15723–15733, https://doi.org/10.1039/d0cp02411b.

[38] K.I. Ishibashi, A. Fujishima, T. Watanabe, K. Hashimoto, Detection of active oxidative species in TiO$_2$ photocatalysis using the fluorescence technique, Electrochem Commun. 2 (2000) 207–210, https://doi.org/10.1016/S1388-2481(00)00006-0.

[39] A. Gómez-Avilés, R.R. Solís, E.M. García-Frutos, J. Bedia, C. Belver, Novel isoreticular UiO-66-NH$_2$ frameworks by N-cycloalkyl functionalization of the 2-aminoterephtalate linker with enhanced solar photocatalytic degradation of acetaminophen, Chem. Eng. J. 461 (2023) 141889, https://doi.org/10.1016/J.CEJ.2023.141889.

[40] M. Qamar, R.B. Elsayed, K.R. Alhooshani, M.I. Ahmed, D.W. Bahnemann, Chemoselective and highly efficient conversion of aromatic alcohols into aldehydes photo-catalyzed by Ag$_3$PO$_4$ in aqueous suspension under simulated sunlight, Catal. Commun. 58 (2015) 34–39, https://doi.org/10.1016/J.CATCOM.2014.08.025.

[41] F. Fina, S.K. Callear, G.M. Carins, J.T.S. Irvine, Structural investigation of graphitic carbon nitride via XRD and neutron diffraction, Chem. Mater. 27 (2015) 2612–2618, https://doi.org/10.1021/ACS.CHEMMATER.5B00411.

[42] X. Li, J. Zhang, L. Shen, Y. Ma, W. Lei, Q. Cui, G. Zou, Preparation and characterization of graphitic carbon nitride through pyrolysis of melamine, Appl. Phys. A Mater. Sci. Process 94 (2009) 387–392, https://doi.org/10.1007/S00339-008-4816-4.

[43] Y. Fei, N. Han, M. Zhang, F. Yang, X. Yu, L. Shi, A. Khataee, W. Zhang, D. Tao, M. Jiang, Facile preparation of visible light-sensitive layered g-C$_3$N$_4$ for photocatalytic removal of organic pollutants, Chemosphere 307 (2022) 135718, https://doi.org/10.1016/J.CHEMOSPHERE.2022.135718.

[44] E. Alwin, W. Nowicki, R. Wojcieszak, M. Zieliński, M. Pietrowski, Elucidating the structure of the graphitic carbon nitride nanomaterials via X-ray photoelectron spectroscopy and X-ray powder diffraction techniques, Dalton Trans. 49 (2020) 12805–12813, https://doi.org/10.1039/D0DT02325F.

[45] Y. Lan, Z. Li, D. Li, G. Yan, Z. Yang, S. Guo, Graphitic carbon nitride synthesized at different temperatures for enhanced visible-light photodegradation of 2-naphthol, Appl. Surf. Sci. 467–468 (2019) 411–422, https://doi.org/10.1016/J.APSUSC.2018.10.152.

[46] X. Bai, S. Yan, J. Wang, L. Wang, W. Jiang, S. Wu, C. Sun, Y. Zhu, A simple and efficient strategy for the synthesis of a chemically tailored g-C$_3$N$_4$ material, J. Mater. Chem. A Mater. 2 (2014) 17521–17529, https://doi.org/10.1039/C4TA02781G.

[47] W. Xing, C. Liu, H. Zhong, Y. Zhang, T. Zhang, C. Cheng, J. Han, G. Wu, G. Chen, Phosphate group-mediated carriers transfer and energy band over carbon nitride for efficient photocatalytic H$_2$ production and removal of rhodamine B, J. Alloy. Compd. 895 (2022) 162772, https://doi.org/10.1016/J.JALLCOM.2021.162772.

[48] P. Gibot, F. Schnell, D. Spitzer, Enhancement of the graphitic carbon nitride surface properties from calcium salts as templates, Microporous Mesoporous Mater. 219 (2016) 42–47, https://doi.org/10.1016/J.MICROMESO.2015.07.026.

[49] X. Yan, P. Yuan, X. Meng, R. Hu, Phosphorus modified graphitic carbon nitride activated by guanidine phosphate enables fast, efficient and selective immobilization of aquatic lead, J. Mol. Liq. 375 (2023) 121339, https://doi.org/10.1016/J.MOLLIQ.2023.121339.

[50] M. Kim, S. Hwang, J.S. Yu, Novel ordered nanoporous graphitic C$_3$N$_4$ as a support for Pt–Ru anode catalyst in direct methanol fuel cell, J. Mater. Chem. 17 (2007) 1656–1659, https://doi.org/10.1039/B702213A.

[51] Z. Yang, C. Qi, P. Yuan, R. Hu, X. Du, M. Cheng, High-efficiency selective removal of U(VI) by phosphate-functionalized graphitic carbon nitride activated using guanidine phosphate, J. Environ. Chem. Eng. 11 (2023) 110272, https://doi.org/10.1016/J.JECE.2023.110272.

[52] X. Wang, X. Li, W. Chen, R. Wang, W. Bian, M.M.F. Choi, Phosphorus doped graphitic carbon nitride nanosheets as fluorescence probe for the detection of baicalein, Spectrochim. Acta A Mol. Biomol. Spectrosc. 198 (2018) 1–6, https://doi.org/10.1016/J.SAA.2018.02.062.

[53] L. Zhang, Q. Liu, Y. Chai, W.L. Dai, Facile construction of phosphate incorporated graphitic carbon nitride with mesoporous structure and superior performance for H$_2$ production, Int. J. Hydrog. Energy 43 (2018) 5591–5602, https://doi.org/10.1016/J.IJHYDENE.2018.01.185.

[54] D.E.C. Corbrjdge, Infra-red analysis of phosphorus compounds, J. Appl. Chem. 6 (1956) 456–465, https://doi.org/10.1002/JCTB.5010061007.

[55] A.M. Puziy, O.I. Poddubnaya, A. Martínez-Alonso, F. Suárez-García, J.M. D. Tascón, Surface chemistry of phosphorus-containing carbons of lignocellulosic origin, Carbon 43 (2005) 2857–2868, https://doi.org/10.1016/J.CARBON.2005.06.014.

[56] D.E.C. Corbridge, E.J. Lowe, The infra-red spectra of some inorganic phosphorus compounds, J. Chem. Soc. (1954) 493–502, https://doi.org/10.1039/JR9540000493.

[57] L.W. Daasch, D.C. Smith, Infrared spectra of phosphorus compounds, Anal. Chem. 23 (1951) 853–868, https://doi.org/10.1021/AC60054A008/ASSET/AC60054A008.FP.PNG_V03.

[58] Y. Wen, D. Qu, L. An, X. Gao, W. Jiang, D. Wu, D. Yang, Z. Sun, Defective g-C$_3$N$_4$ prepared by the NaBH$_4$ reduction for high-performance H$_2$ production, ACS Sustain Chem. Eng. 7 (2019) 2343–2349, https://doi.org/10.1021/ACSSUSCHEMENG.8B05124.

[59] R.R. Solís, M.A. Quintana, G. Blázquez, M. Calero, M.J. Muñoz-Batista, Ruthenium deposited onto graphitic carbon modified with boron for the intensified photocatalytic production of benzaldehyde, Catal. Today 423 (2023) 114266, https://doi.org/10.1016/J.CATTOD.2023.114266.

[60] J. Su, Y. Zhao, J. Xi, Phosphorus-doped carbon nitride as powerful electrocatalyst for high-power vanadium flow battery, Electrochim. Acta 286 (2018) 22–28, https://doi.org/10.1016/J.ELECTACTA.2018.08.044.

[61] R. Škuta, V. Matějka, A. Smýkalová, D. Cvejn, R. Gabor, M. Kormunda, B. Smetana, V. Novák, P. Praus, On P-doping of graphitic carbon nitride with hexachlorotriphosphazene as a source of phosphorus, Appl. Surf. Sci. 552 (2021) 149490, https://doi.org/10.1016/J.APSUSC.2021.149490.

[62] F. Zhang, J. Li, H. Wang, Y. Li, Y. Liu, Q. Qian, X. Jin, X. Wang, J. Zhang, G. Zhang, Realizing synergistic effect of electronic modulation and nanostructure engineering over graphitic carbon nitride for highly efficient visible-light H$_2$ production coupled with benzyl alcohol oxidation, Appl. Catal. B 269 (2020) 118772, https://doi.org/10.1016/J.APCATB.2020.118772.

[63] A.P. Dementjev, A. De Graaf, M.C.M. Van de Sanden, K.I. Maslakov, A. V. Naumkin, A.A. Serov, X-ray photoelectron spectroscopy reference data for identification of the C$_3$N$_4$ phase in carbon–nitrogen films, Diam. Relat. Mater. 9 (2000) 1904–1907, https://doi.org/10.1016/S0925-9635(00)00345-9.

[64] U. Caudillo-Flores, D. Rodríguez-Padrón, M.J. Muñoz-Batista, A. Kubacka, R. Luque, M. Fernández-García, Facile synthesis of B/g-C$_3$N$_4$ composite materials for the continuous-flow selective photo-production of acetone, Green Chem. 22 (2020) 4975–4984, https://doi.org/10.1039/D0GC01326A.

[65] H. Xu, Z. Wu, Y. Wang, C. Lin, Enhanced visible-light photocatalytic activity from graphene-like boron nitride anchored on graphitic carbon nitride sheets, J. Mater. Sci. 52 (2017) 9477–9490, https://doi.org/10.1007/S10853-017-1167-6.

[66] Y. Duan, Y. Wang, L. Gan, J. Meng, Y. Feng, K. Wang, K. Zhou, C. Wang, X. Han, X. Zhou, Amorphous carbon nitride with three coordinate nitrogen (N3$_C$) vacancies for exceptional NO$_x$ abatement in visible light, Adv. Energy Mater. 11 (2021) 2004001, https://doi.org/10.1002/AENM.202004001.

[67] J. Wu, X. Zheng, C. Jin, J. Tian, R. Yang, Ternary doping of phosphorus, nitrogen, and sulfur into porous carbon for enhancing electrocatalytic oxygen reduction, Carbon 92 (2015) 327–338, https://doi.org/10.1016/J.CARBON.2015.05.013.

[68] Y. Zhang, T. Mori, J. Ye, M. Antonietti, Phosphorus-doped carbon nitride solid: enhanced electrical conductivity and photocurrent generation, J. Am. Chem. Soc. 132 (2010) 6294–6295, https://doi.org/10.1021/JA101749Y/SUPPL_FILE/JA101749Y_SI_002.PDF.

[69] Y.P. Zhu, T.Z. Ren, Z.Y. Yuan, Mesoporous phosphorus-doped g-C$_3$N$_4$ nanostructured flowers with superior photocatalytic hydrogen evolution performance, ACS Appl. Mater. Interfaces 7 (2015) 16850–16856, https://doi.org/10.1021/ACSAMI.5B04947.

[70] L. Zhang, X. Chen, J. Guan, Y. Jiang, T. Hou, X. Mu, Facile synthesis of phosphorus doped graphitic carbon nitride polymers with enhanced visible-light photocatalytic activity, Mater. Res. Bull. 48 (2013) 3485–3491, https://doi.org/10.1016/J.MATERRESBULL.2013.05.040.

[71] S. Guo, Z. Deng, M. Li, B. Jiang, C. Tian, Q. Pan, H. Fu, Phosphorus-doped carbon nitride tubes with a layered micro-nanostructure for enhanced visible-light photocatalytic hydrogen evolution, Angew. Chem. Int. Ed. 55 (2016) 1830–1834, https://doi.org/10.1002/ANIE.201508505.

[72] J. Li, Y. Qi, Y. Mei, S. Ma, Q. Li, B. Xin, T. Yao, J. Wu, Construction of phosphorus-doped carbon nitride/phosphorus and sulfur co-doped carbon nitride isotype heterojunction and their enhanced photoactivity, J. Colloid Interface Sci. 566 (2020) 495–504, https://doi.org/10.1016/J.JCIS.2020.01.102.

[73] J. Huang, D. Li, R. Li, Q. Zhang, T. Chen, H. Liu, Y. Liu, W. Lv, G. Liu, An efficient metal-free phosphorus and oxygen co-doped g-C$_3$N$_4$ photocatalyst with enhanced visible light photocatalytic activity for the degradation of fluoroquinolone antibiotics, Chem. Eng. J. 374 (2019) 242–253, https://doi.org/10.1016/J.CEJ.2019.05.175.

[74] K.J. Gaskell, P.M.A. Sherwood, Sodium phosphate dodecahydrate (Na$_3$PO$_4$·12H$_2$O) by XPS, Surf. Sci. Spectra 9 (2002) 75–82, https://doi.org/10.1116/11.20030103.

[75] B. Cai, R. Kang, D. Guo, J. Feng, T. Ma, H. Pan, An eco-friendly acidic catalyst phosphorus-doped graphitic carbon nitride for efficient conversion of fructose to 5-Hydroxymethylfurfural, Renew. Energy 199 (2022) 1629–1638, https://doi.org/10.1016/J.RENENE.2022.09.050.

[76] D. Jang, S. Lee, N.H. Kwon, T. Kim, S. Park, K.Y. Jang, E. Yoon, S. Choi, J. Han, T.W. Lee, J. Kim, S.J. Hwang, S. Park, Preparation of carbon nitride nanotubes with P-doping and their photocatalytic properties for hydrogen evolution, Carbon 208 (2023) 290–302, https://doi.org/10.1016/J.CARBON.2023.03.038.

[77] S. Wang, F. He, X. Zhao, J. Zhang, Z. Ao, H. Wu, Y. Yin, L. Shi, X. Xu, C. Zhao, S. Wang, H. Sun, Phosphorous doped carbon nitride nanobelts for photodegradation of emerging contaminants and hydrogen evolution, Appl. Catal. B 257 (2019) 117931, https://doi.org/10.1016/J.APCATB.2019.117931.

[78] Y. Zhou, L. Zhang, J. Liu, X. Fan, B. Wang, M. Wang, W. Ren, J. Wang, M. Li, J. Shi, Brand new P-doped g-C$_3$N$_4$: enhanced photocatalytic activity for H$_2$ evolution and Rhodamine B degradation under visible light, J. Mater. Chem. A Mater. 3 (2015) 3862–3867, https://doi.org/10.1039/C4TA05292G.

[79] Y. jie Sun, J. yan He, D. Zhang, X. jing Wang, J. Zhao, R. hong Liu, F. tang Li, Simultaneous construction of dual-site phosphorus modified g-C$_3$N$_4$ and its synergistic mechanism for enhanced visible-light photocatalytic hydrogen evolution, Appl. Surf. Sci. 517 (2020) 146192, https://doi.org/10.1016/J.APSUSC.2020.146192.

[80] J. Ran, T.Y. Ma, G. Gao, X.W. Du, S.Z. Qiao, Porous P-doped graphitic carbon nitride nanosheets for synergistically enhanced visible-light photocatalytic H$_2$ production, Energy Environ. Sci. 8 (2015) 3708–3717, https://doi.org/10.1039/C5EE02650D.

[81] H. Bin Fang, X.H. Zhang, J. Wu, N. Li, Y.Z. Zheng, X. Tao, Fragmented phosphorus-doped graphitic carbon nitride nanoflakes with broad sub-bandgap absorption for highly efficient visible-light photocatalytic hydrogen evolution, Appl. Catal. B 225 (2018) 397–405, https://doi.org/10.1016/J.APCATB.2017.11.080.

[82] H. Yang, Y. Zhou, Y. Wang, S. Hu, B. Wang, Q. Liao, H. Li, J. Bao, G. Ge, S. Jia, Three-dimensional flower-like phosphorus-doped g-C$_3$N$_4$ with a high surface area for visible-light photocatalytic hydrogen evolution, J. Mater. Chem. A Mater. 6 (2018) 16485–16494, https://doi.org/10.1039/C8TA05723K.

[83] L.L. Liu, F. Chen, J.H. Wu, W.W. Li, J.J. Chen, H.Q. Yu, Fine tuning of phosphorus active sites on g-C$_3$N$_4$ nanosheets for enhanced photocatalytic decontamination, J. Mater. Chem. A Mater. 9 (2021) 10933–10944, https://doi.org/10.1039/D1TA01537K.

[84] H. Li, N. Zhang, F. Zhao, T. Liu, Y. Wang, Facile fabrication of a novel Au/phosphorus-doped g-C$_3$N$_4$ photocatalyst with excellent visible light photocatalytic activity, Catalysts 10 (2020) 701, https://doi.org/10.3390/CATAL10060701.

[85] S. Hu, L. Ma, J. You, F. Li, Z. Fan, G. Lu, D. Liu, J. Gui, Enhanced visible light photocatalytic performance of g-C$_3$N$_4$ photocatalysts co-doped with iron and phosphorus, Appl. Surf. Sci. 311 (2014) 164–171, https://doi.org/10.1016/J.APSUSC.2014.05.036.

[86] F. Ding, Y.P. Feng, Structural and electronic properties of C$_{3}$N$_{4−n}$P$_n$ (n=0,1,2,3,4), Comput. Mater. Sci. 30 (2004) 364–370, https://doi.org/10.1016/J.COMMATSCI.2004.02.032.

[87] H. Sun, S.J. Park, Phosphorus-doped g-C$_3$N$_4$/SnS nanocomposite for efficient photocatalytic reduction of aqueous Cr(VI) under visible light, Appl. Surf. Sci. 531 (2020) 147325, https://doi.org/10.1016/J.APSUSC.2020.147325.

[88] S. Guo, Y. Tang, Y. Xie, C. Tian, Q. Feng, W. Zhou, B. Jiang, P-doped tubular g-C$_3$N$_4$ with surface carbon defects: universal synthesis and enhanced visible-light photocatalytic hydrogen production, Appl. Catal. B 218 (2017) 664–671, https://doi.org/10.1016/J.APCATB.2017.07.022.

[89] J. Feng, D. Zhang, H. Zhou, M. Pi, X. Wang, S. Chen, Coupling P nanostructures with P-doped g-C$_3$N$_4$ as efficient visible light photocatalysts for H$_2$ evolution and RhB degradation, ACS Sustain Chem. Eng. 6 (2018) 6342–6349, https://doi.org/10.1021/ACSSUSCHEMENG.8B00140.

[90] C. Hardacre, E.A. Mullan, D.W. Rooney, J.M. Thompson, Use of a rotating disc reactor to investigate the heterogeneously catalysed oxidation of cinnamyl alcohol in toluene and ionic liquids, J. Catal. 232 (2005) 355–365, https://doi.org/10.1016/J.JCAT.2005.03.014.

[91] L. Samiolo, M. Valigi, D. Gazzoli, R. Amadelli, Photo-electro catalytic oxidation of aromatic alcohols on visible light-absorbing nitrogen-doped TiO$_2$, Electrochim. Acta 55 (2010) 7788–7795, https://doi.org/10.1016/J.ELECTACTA.2009.04.044.

[92] M.S. Alam, B.S.M. Rao, E. Janata, OH reactions with aliphatic alcohols: evaluation of kinetics by direct optical absorption measurement. A pulse radiolysis study, Radiat. Phys. Chem. 67 (2003) 723–728, https://doi.org/10.1016/S0969-806X(03)00310-4.

[93] E. Bouleghlimat, D. Bethell, P.R. Davies, The photocatalytic destruction of cinnamic acid and cinnamyl alcohol: mechanism and the effect of aqueous ions, Chemosphere 251 (2020) 126469, https://doi.org/10.1016/J.CHEMOSPHERE.2020.126469.

[94] M. Qamar, R.B. Elsayed, K.R. Alhooshani, M.I. Ahmed, D.W. Bahnemann, Chemoselective and highly efficient conversion of aromatic alcohols into aldehydes photo-catalyzed by Ag$_3$PO$_4$ in aqueous suspension under simulated sunlight, Catal. Commun. 58 (2015) 34–39, https://doi.org/10.1016/J.CATCOM.2014.08.025.

[95] K. Srinivasu, B. Modak, S.K. Ghosh, Porous graphitic carbon nitride: a possible metal-free photocatalyst for water splitting, J. Phys. Chem. C 118 (2014) 26479–26484, https://doi.org/10.1021/JP506538D/SUPPL_FILE/JP506538D_SI_001.PDF.

[96] J. Wang, Z. Bian, J. Zhu, H. Li, Ordered mesoporous TiO$_2$ with exposed (001) facets and enhanced activity in photocatalytic selective oxidation of alcohols, J. Mater. Chem. A Mater. 1 (2012) 1296–1302, https://doi.org/10.1039/C2TA00035K.

[97] B.H.J. Bielski, D.E. Cabelli, R.L. Arudi, A.B. Ross, Reactivity of HO$_2$/O$_2^-$ radicals in aqueous solution, J. Phys. Chem. Ref. Data 14 (1985) 1041–1100, https://doi.org/10.1063/1.555739.

[98] M. Anbar, P. Neta, A compilation of specific bimolecular rate constants for the reactions of hydrated electrons, hydrogen atoms and hydroxyl radicals with inorganic and organic compounds in aqueous solution, Int. J. Appl. Radiat. Isot. 18 (1967) 493–523, https://doi.org/10.1016/0020-708X(67)90115-9.

[99] M.Nien Schuchmann, E. Bothe, J. von Sonntag, C. von Sonntag, Reaction of OH radicals with benzoquinone in aqueous solutions. A pulse radiolysis study, J. Chem. Soc. Perkin Trans. 2 (1998) 791–796, https://doi.org/10.1039/A708772A.

[100] S. Garg, A.L. Rose, T.D. Waite, Production of reactive oxygen species on photolysis of dilute aqueous quinone solutions, Photochem. Photobiol. 83 (2007) 904–913, https://doi.org/10.1111/J.1751-1097.2007.00075.X.

[101] A.E. Alegría, A. Ferrer, G. Santiago, E. Sepúlveda, W. Flores, Photochemistry of water-soluble quinones. Production of the hydroxyl radical, singlet oxygen and the superoxide ion, J. Photochem. Photobiol. A Chem. 127 (1999) 57–65, https://doi.org/10.1016/S1010-6030(99)00138-0.

[102] W. Bors, M. Saran, C. Michel, Pulse-radiolytic investigations of catechols and catecholamines II. Reactions of Tiron with oxygen radical species, Biochem. Biophys. Acta (BBA) Gen. Subj. 582 (1979) 537–542, https://doi.org/10.1016/0304-4165(79)90145-4.

[103] Y. Song, H. Wang, G. Liu, H. Wang, L. Li, Y. Yu, L. Wu, Constructing surface synergistic effect in Cu-Cu$_2$O hybrids and monolayer H$_{1.4}$Ti$_{1.65}$O$_4$·H$_2$O nanosheets for selective cinnamyl alcohol oxidation to cinnamaldehyde, J. Catal. 370 (2019) 461–469, https://doi.org/10.1016/J.JCAT.2019.01.016.

[104] B.R. Shah, U.D. Patel, Mechanistic aspects of photocatalytic degradation of Lindane by TiO$_2$ in the presence of Oxalic acid and EDTA as hole-scavengers, J. Environ. Chem. Eng. 9 (2021) 105458, https://doi.org/10.1016/J.JECE.2021.105458.

[105] B.G. Ershov, E. Janata, M.S. Alam, A.V. Gordeev, A pulse radiolysis study of the reactions of the hydrated electron and hydroxyl radical with the oxalate ion in neutral aqueous solution, High. Energy Chem. 42 (2008) 1–6, https://doi.org/10.1134/s0018143908010013.

[106] B.R. Shah, U.D. Patel, Mechanistic aspects of photocatalytic degradation of Lindane by TiO2 in the presence of Oxalic acid and EDTA as hole-scavengers, J. Environ. Chem. Eng. 9 (2021) 105458, https://doi.org/10.1016/J.JECE.2021.105458.

[107] X. Dai, M. Xie, S. Meng, X. Fu, S. Chen, Coupled systems for selective oxidation of aromatic alcohols to aldehydes and reduction of nitrobenzene into aniline using CdS/g-C$_3$N$_4$ photocatalyst under visible light irradiation, Appl. Catal. B 158–159 (2014) 382–390, https://doi.org/10.1016/J.APCATB.2014.04.035.

[108] W.H. Koppenol, D.M. Stanbury, P.L. Bounds, Electrode potentials of partially reduced oxygen species, from dioxygen to water, Free Radic. Biol. Med. 49 (2010) 317–322, https://doi.org/10.1016/J.FREERADBIOMED.2010.04.011.

[109] P.M. Wood, The potential diagram for oxygen at pH 7, Biochem. J. 253 (1988) 287–289, https://doi.org/10.1042/BJ2530287.

[110] I.B. Niklasson, T. Delaine, M.N. Islam, R. Karlsson, K. Luthman, A.T. Karlberg, Cinnamyl alcohol oxidizes rapidly upon air exposure, Contact Dermat. 68 (2013) 129–138, https://doi.org/10.1111/COD.12009.

[111] E. Bouleghlimat, D. Bethell, P.R. Davies, The photocatalytic destruction of cinnamic acid and cinnamyl alcohol: mechanism and the effect of aqueous ions, Chemosphere 251 (2020) 126469, https://doi.org/10.1016/J.CHEMOSPHERE.2020.126469.

[112] G. Wu, G.L. Brett, E. Cao, A. Constantinou, P. Ellis, S. Kuhn, G.J. Hutchings, D. Bethell, A. Gavriilidis, Oxidation of cinnamyl alcohol using bimetallic Au–Pd/TiO$_2$ catalysts: a deactivation study in a continuous flow packed bed

microreactor, Catal. Sci. Technol. 6 (2016) 4749–4758, https://doi.org/10.1039/C6CY00232C.

[113] Y. Wang, P. Prinsen, F. Mangin, A. Yepez, A. Pineda, E. Rodríguez-Castellón, M. R. Hasan Shah Gilani, G. Xu, C. Len, R. Luque, Mechanistic insights into the microwave-assisted cinnamyl alcohol oxidation using supported iron and

palladium catalysts, Mol. Catal. 474 (2019) 110409, https://doi.org/10.1016/J.MCAT.2019.110409.

[114] L.B. Ellis, L.P. Wackett, Use of the University of Minnesota biocatalysis/biodegradation database for study of microbial degradation, Microb. Inform. Exp. 2 (2012) 1–10, https://doi.org/10.1186/2042-5783-2-1.